

REPORT DOCUMENTATION PAGE

Form Approved
OMB No. 074-0188

Public reporting burden for this collection of information is estimated to average 1 hour per response, including the time for reviewing instructions, searching existing data sources, gathering and maintaining the data needed, and completing and reviewing this collection of information. Send comments regarding this burden estimate or any other aspect of this collection of information, including suggestions for reducing this burden to Washington Headquarters Services, Directorate for Information Operations and Reports, 1215 Jefferson Davis Highway, Suite 1204, Arlington, VA 22202-4302, and to the Office of Management and Budget, Paperwork Reduction Project (0704-0188), Washington, DC 20503

1. AGENCY USE ONLY (Leave blank)		2. REPORT DATE APRIL 1998	3. REPORT TYPE AND DATES COVERED FINAL TECHNICAL REPORT 8/1/96 - 11/30/97	
4. TITLE AND SUBTITLE LARGE EDDY SIMULATION OF TURBULENT FLOW OVER AN AIRFOIL USING BOTH STRUCTURED AND UNSTRUCTURED GRIDS			5. FUNDING NUMBERS F49520-96-1-0420	
6. AUTHOR(S) PROF. PARVIZ MOIN				
7. PERFORMING ORGANIZATION NAME(S) AND ADDRESS(ES) STANFORD UNIVERSITY MECHANICAL ENGINEERING FLOW PHYSICS & COMPUTATION DIVISION STANFORD, CA 94305-3030			8. PERFORMING ORGANIZATION REPORT NUMBER	
9. SPONSORING / MONITORING AGENCY NAME(S) AND ADDRESS(ES) AFOSR DR. LEONIDAS SAKELL 110 DUNCAN AVE., STE. B115 BOLLING AFB, DC 20332-0001			10. SPONSORING / MONITORING AGENCY REPORT NUMBER 2DJA588	
11. SUPPLEMENTARY NOTES				
12a. DISTRIBUTION / AVAILABILITY STATEMENT APPROVED FOR PUBLIC RELEASE. DISTRIBUTION IS UNLIMITED				12b. DISTRIBUTION CODE
13. ABSTRACT (Maximum 200 Words) This report describes the application of Large Eddy Simulations (LES) to turbulent flow over an airfoil. Two different approaches have been used, a second-order finite-difference solver on structured grid and a finite-element solver on unstructured grid. Results are presented for the flow around a NACA 4412 airfoil at maximum lift. The diversity of flow characteristics encountered in this flow include laminar, transitional and turbulent boundary layers, flow separation, unstable free shear layers and a wake. While Reynolds-averaged Navier-Stokes simulations (RANS) have had some success when tuned to flows dominated by one such flow characteristic, this variety of flow features taxes the presently available RANS models and presents an excellent opportunity to validate the utility of the dynamic SGS model for LES. Work has also been conducted on high order methods, both for the unstructured and the structured approach.				
14. SUBJECT TERMS LARGE EDDY SIMULATION, TURBULENT FLOW, TURBULENCE, AIRFOIL, STRUCTURED GRID, UNSTRUCTURED GRID				15. NUMBER OF PAGES 50
				16. PRICE CODE
17. SECURITY CLASSIFICATION OF REPORT UNCLASSIFIED	18. SECURITY CLASSIFICATION OF THIS PAGE UNCLASSIFIED	19. SECURITY CLASSIFICATION OF ABSTRACT UNCLASSIFIED	20. LIMITATION OF ABSTRACT	

19980514 105

DTIC QUALITY INSPECTED 4

Final Technical Report for the period August 1, 1996 - November 30, 1997 for the grant
entitled:

Large Eddy Simulation of Turbulent Flow Over an Airfoil Using Both Structured and Unstructured Grids

Approved for public release;
distribution unlimited.

AFOSR (AFSC)
AFOTIC
has been reviewed and is
release IAW AFR 190-12
unlimited.
Manager

Parviz Moin

Stanford University

Mechanical Engineering, Flow Physics & Computation Division

Stanford, CA 94305-3030

Prepared with the support of the
Air Force Office of Scientific Research
under AFOSR Grant: F49520-96-1-0420

Four technical reports covering the accomplishments in this project are attached. Below we provide an executive summary of the work performed.

Objectives

- Perform a Large Eddy Simulation of a flow around an airfoil at maximum lift using both structured and unstructured grids.
- Perform efficient parallel implementation of the codes.

The results of the first stage of the investigations, using both a finite-difference method on a structured mesh and a finite-element method on an unstructured mesh, differed considerably from each other and from the available experimental data. Differences were found with respect to the occurrence of transition near the suction peak and with respect to the amount of backflow near the trailing edge. To identify the cause of the mismatch, we addressed some important issues:

- The sensitivity of the overall flow to details in the nose section, in particular to the transition strip.
- The effect of windtunnel walls.
- The spanwise domain size.

To answer these questions, we selected the finite-element code due to its ability to easily handle complex geometry and local refinement of the mesh. At the same time, we started the porting of the structured code on parallel machines.

Accomplishment and future plans

Unstructured code

This code solves the compressible Navier-Stokes equations on an unstructured grid via a Galerkin/least-squares stabilized finite element method. The code has been ported to the IBM SP2. The code now uses MPI, a communication standard that is more widely used than that of the original code, which should

facilitate the port to other platforms. As indicated in the attached technical reports, the calculations were in disagreement with the experimental data. Several possible causes for the discrepancies were investigated.

1. Effect of wind tunnel walls and transition strip

In the experiment, a strip of tape with serrations cut into the edge on the upstream side was used. The serrated tape has been modeled in a coarse fashion by our current simulation as can be seen in Appendix 4, Fig. 1. The tape is effectively a forward facing step (with serrations) of height $\delta_{99}/4$, followed by a backward facing step.

The blockage effect of the wind tunnel walls has also been included in the recent calculations. Note that the boundary layers on the walls are not simulated; rather, slip boundary conditions are applied on the wind tunnel walls as can be seen in Appendix 4, Fig. 2.

These two effects were studied separately for a short period of time (not sufficient for converged statistics in the trailing edge region), and agreement with experiments was seen to improve in both cases. The effect of the walls was somewhat greater than that of the transition strip. The results of this simulation can be seen in Appendix 4, Fig. 3, where the velocity profiles of the new simulation (with wind tunnel walls and transition strip) are compared to the original simulation. Note the large increase in the degree of separation. This study is being continued by Prof. Jansen at Rensselaer Polytechnic Institute under a separate AFOSR contract.

2. More spanwise domain studies

Based on the findings in the previous section, more attention was given to the spanwise domain effects. Since the resolution changed at the same time as the expansion of the domain, it is difficult to isolate the two effects. For this reason the first study maintained 5% chord domain width and improved the resolution in the second half of the airfoil where the solution has shown some change. These calculations are being carried out by Prof. Jansen.

3. Higher order methods

Given the number of points that are required to obtain a grid-independent solution, it seems clear that higher order methods should be explored. This is straightforward, but non-trivial, to do with the finite element method. There

is another benefit to higher order methods besides the obvious one of higher accuracy. The higher order methods will have a more complete representation of the residual error of the discrete approximation and, therefore, the scheme will be less dissipative.

A fourth-order finite difference code with suitable conservation properties has also been developed. This code has been tested in turbulent channel flow.

Structured code

The code is based on a second-order finite difference method which solves, on a staggered mesh, the three-dimensional incompressible Navier-Stokes equations in primitive variables (velocity and pressure) and in generalized coordinates on a spanwise periodic domain. The solution is advanced in time by a semi-implicit third-order Runge-Kutta scheme. The SGS model implemented is a version of the dynamic model suitable for application in generalized coordinates, with the coefficient averaged in the spanwise direction. The use of a C-mesh allows a better resolution in the wake region and simplifies the imposition of outflow boundary conditions.

The serial code was optimized on a Cray C90. Different strategies should be used on different processors found in parallel computers, where performance is heavily affected by the presence of memory hierarchies. The array layout has been rearranged and the code has been optimized on a single SP2 processor.

The parallel formulation employs spatial decomposition of the overall grid into sub blocks that are assigned to separate processors and use MPI as the message-passing programming interface. A 2-D domain decomposition in the plane of generalized coordinates is used in order to distribute data across concurrent processors. The 2-D decomposition will allow the use of a large number of processors (64,128) with a good ratio between surfaces and volumes of the domains. A flexible decomposition has been implemented in which each domain could have a different size (the 2-D decomposition is the product of two general 1-D decompositions) and different boundary conditions.

The solution at points shared by neighboring processors is updated between each sub step by means of a message exchange. Due to the staggered grid and generalized coordinates, each block needs two layers of "ghost" cells. Some important issues such as the solution of the Poisson equation necessary to project the velocity field in a divergence-free space have been addressed.

A parallel multigrid solver has been implemented using MPI as the communication library. This solver utilizes a parallel tridiagonal solver, and it is capable of full-coarsening and semi-coarsening.

The parallel code will permit the use of fine grids that will avoid unphysical oscillation observed when the mesh is too coarse.

APPENDIX 1. Preliminary large-eddy simulations of flow around a NACA 4412 airfoil using unstructured grids

By Kenneth Jansen

1. Motivation and objectives

Large-eddy simulation (LES) has matured to the point where application to complex flows is desirable. The extension to higher Reynolds numbers leads to an impractical number of grid points with existing structured-grid methods. Furthermore, most real world flows are rather difficult to represent geometrically with structured grids. Unstructured-grid methods offer a release from both of these constraints. However, just as it took many years for structured-grid methods to be well understood and reliable tools for LES, unstructured-grid methods must be carefully studied before we can expect them to attain their full potential.

In the past two years, important building blocks have been put into place making possible a careful study of LES on unstructured grids. The first building block was an efficient mesh generator which allowed the placement of points according to smooth variation of physical length scales. This variation of length scales is in all three directions independently, which allows a large reduction in points when compared to structured-grid methods, which can only vary length scales in one direction at a time. The second building block was the development of a dynamic model appropriate for unstructured grids. The principle obstacle was the development of an unstructured-grid filtering operator. New filtering operators were developed in Jansen (1994). In the past year, some of these filters have been implemented into a highly parallelized finite element code based on the Galerkin/least-squares finite element method (see Jansen *et al.* (1993) and Johan *et al.* (1992)).

We have chosen the NACA 4412 airfoil at maximum lift as the first simulation for a variety of reasons. First, it is a problem of significant interest since it would be the first LES of an aircraft component. Second, this flow has been the subject of three experimental studies (Coles and Wadcock (1979), Hasting and Williams (1987), and Wadcock (1987)). The first study found the maximum lift angle to be 13.87° . The later studies found the angle to be 12° . Wadcock reports in the later study that the early data agree very well with his new data at 12° , suggesting that the early experiment suffered from a non-parallel mean flow in the Caltech wind tunnel. It should be pointed out that the Reynolds-averaged simulations are usually run at 13.87° and do not agree with the data when run at 12° as will be shown later in this study. It is hoped that LES can clarify this controversy. The third reason for considering this flow is the variety of flow features which provide an important test of the dynamic model. Starting from the nose where the flow stagnates, thin laminar boundary layers are formed in a very favorable pressure gradient. This pressure

gradient soon turns adverse, driving the flow toward a leading edge separation. Only the onset of turbulence can cause the flow to remain attached or to reattach if it did separate. The persistent adverse pressure gradient eventually drives the turbulent flow to separate in the last 20 percent of chord. The separation bubble is closed near the trailing edge as the retarded upper surface boundary layer interacts with the very thin lower surface boundary layer. The large difference in boundary layers creates a challenging wake to simulate. Only the dynamic model can be expected to perform satisfactorily in this variety of situations: from the laminar regions where it must not modify the flow at all to the turbulent boundary layers and wake where it must represent a wide variety of subgrid-scale structures.

The flow configuration we have chosen is that of Wadcock (1987) at Reynolds number based on chord $Re_c = u_\infty c / \nu = 1.64 \times 10^6$, Mach number $M = 0.2$, and 12° angle of attack.

2. Accomplishments

2.1 Dynamic model implemented and tested

The only obstacle to implementing a dynamic model on unstructured grids is extension of the filtering operator. Four filtering operators were proposed in Jansen (1994). Two of these models were implemented and compared using a simple analytic velocity field for which the filtered values can be determined exactly. From this test, the generalized top-hat was found to be the most accurate, and all subsequent calculations have been carried out using this filter.

2.2 Simulations

A series of simulations has been performed in the last year to develop experience with this new approach. The first simulation was intentionally very coarse as we hoped to improve the mesh selectively and develop an understanding of the sensitivity of the solution to the grid improvements.

2.2.1 First simulation

The first simulation was performed on a very coarse mesh. The near-wall grid did not attempt to resolve the near-wall layer accurately in the first 20 percent of chord and only marginally resolved the remaining flow ($\Delta_x^+ = 300$, $\Delta_z^+ = 80$) at the wall. The grid was coarsened in the streamwise and spanwise directions coming off the wall as suggested by Chapman (1979). The resulting coefficient of pressure distribution was reasonably well predicted on this mesh (see Fig. 1), but the velocity profiles showed poor agreement with the experiment.

2.2.2 Improvement of outer layer

Careful scrutiny of the mesh revealed that the strategy of coarsening in the streamwise direction coming off the wall was inappropriate at this Reynolds number. The inner-layer spacing, Δ , scales on wall units.

$$\frac{\Delta}{c} \propto \frac{\nu}{u_\tau c} = \frac{\sqrt{2}}{Re_c \sqrt{C_f}}$$

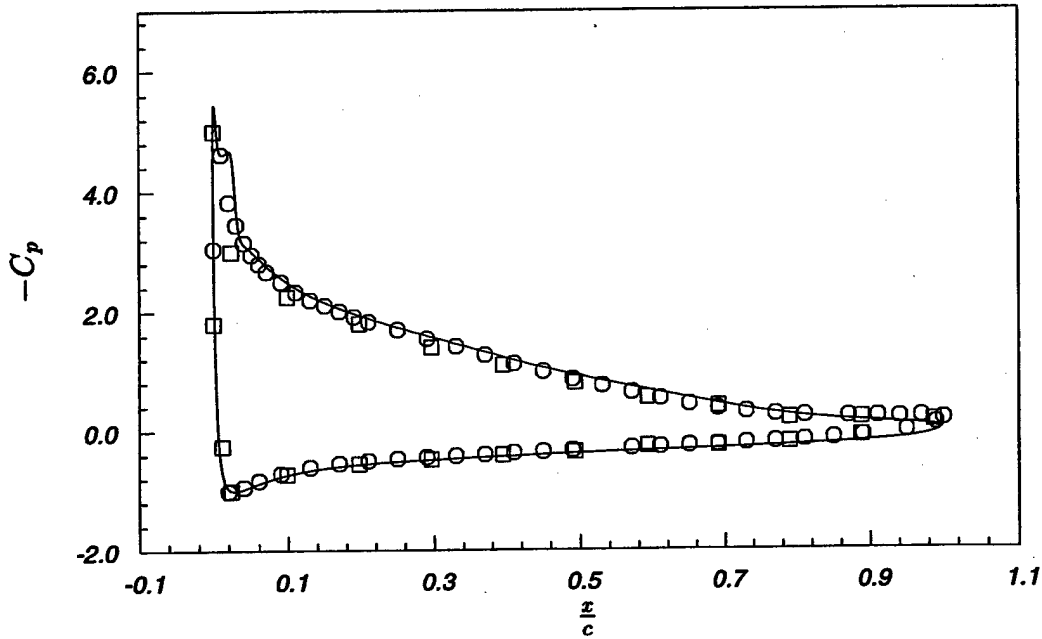


FIGURE 1. Coefficient of pressure along the airfoil surface. LES —, Hastings and Williams \circ , Wadcock (1987) \square .

Here, ν , is the kinematic viscosity, c is the chord length, and u_τ is the friction velocity defined to be the square root of the coefficient of friction, C_f , over two. The outer-layer spacing scales on the boundary layer thickness, δ_{99} . It is reasonable to expect the large eddies in the outer part of the boundary layer to be of order δ_{99} , and therefore the outer-layer spacing, in all directions, should never exceed

$$\Delta = \frac{\delta_{99}}{5}$$

By using Wadcock's experimental data for the C_f and δ_{99} , one can compare these two resolution restrictions as is done in Fig. 2. This figure contains three curves. The solid curve describes the variation of a 200 wall-unit spacing (which can be associated with the streamwise spacing near the wall) over the upper surface where the boundary layer is attached. The dashed curve describes the same variation of 50 wall units (which can be associated with spanwise spacing near the wall). The chain dash curve is the outer-layer spacing as described above. Several points can be made in this figure. First, all three curves change by over an order of magnitude from the tip to the tail region. This illustrates how an unstructured grid saves points by matching resolution to the local changes in the length scales in the streamwise direction. For example, a structured grid would be forced to carry the fine spanwise resolution required near the nose through the entire domain. Second, when comparing the near-wall spanwise resolution to the outer-layer resolution, it is clear that coarsening the spanwise resolution as the distance from the wall increases is justified. The final point, apparent from this figure, is that coarsening

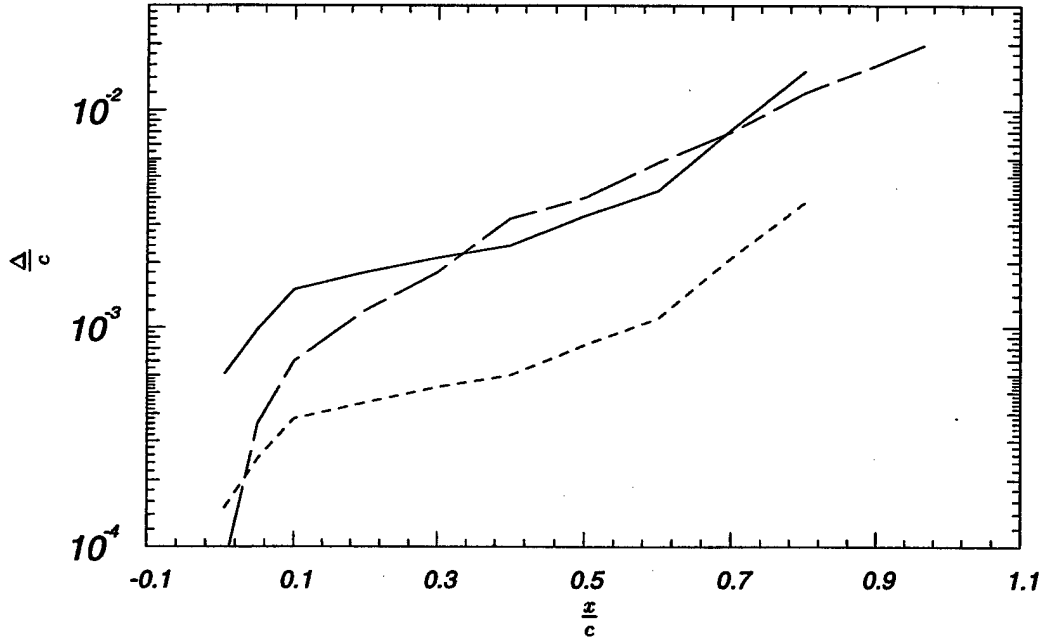


FIGURE 2. Comparison of length scales over the airfoil surface. 200 wall units (streamwise near-wall spacing) —, $\delta_{99}/5$ (outer-layer spacing) ---, 50 wall units (spanwise near-wall spacing) - - - -.

of the streamwise resolution in the outer layer is not justified. In fact, over much of the airfoil surface the outer-layer grid resolution is more restrictive than the inner-layer resolution. The choices of 200 wall units and 5 points per boundary layer thickness are somewhat arbitrary, but they are believed to be comparable in their degree of coarseness. It is interesting to observe that the crossover between these two curves corresponds to $Re_\tau = (u_\tau \delta_{99}/\nu) = 1000$. Therefore, when above 1000, the inner-layer resolution is the most restrictive. Otherwise, the outer-layer resolution is the most restrictive. Only at higher Reynolds numbers will coarsening in the streamwise direction be justified.

Considering the above discussion, a new mesh was made where the coarsening of the streamwise spacing was delayed until outside of the boundary layer. This resulted in a mesh with nearly twice as many points as the previous simulation. It also resulted in a rather dramatic change in the early boundary layer structure. It seems that the improved resolution of the outer layer allowed a better resolution of the leading edge separation. The new simulation led to a train of spanwise coherent vortices. These vortices broke down into turbulence at about 10 percent of chord.

The persistence of the spanwise coherent vortices was not in line with the experiments which were all tripped. Some evidence as to the importance of the tripping can be seen in Fig. 3 where we compare the surface coefficient of pressure distribution from the free transition simulation to two experimental data sets from Hastings and Williams (1987). The square data set was taken without a transition strip while the circle data set was taken with a transition strip. Our simulation shows rather

good agreement with the free transition. Unfortunately, all velocity and Reynolds stress data were taken with the transition strip in place and agreement with these quantities is substantially worse than with C_p .

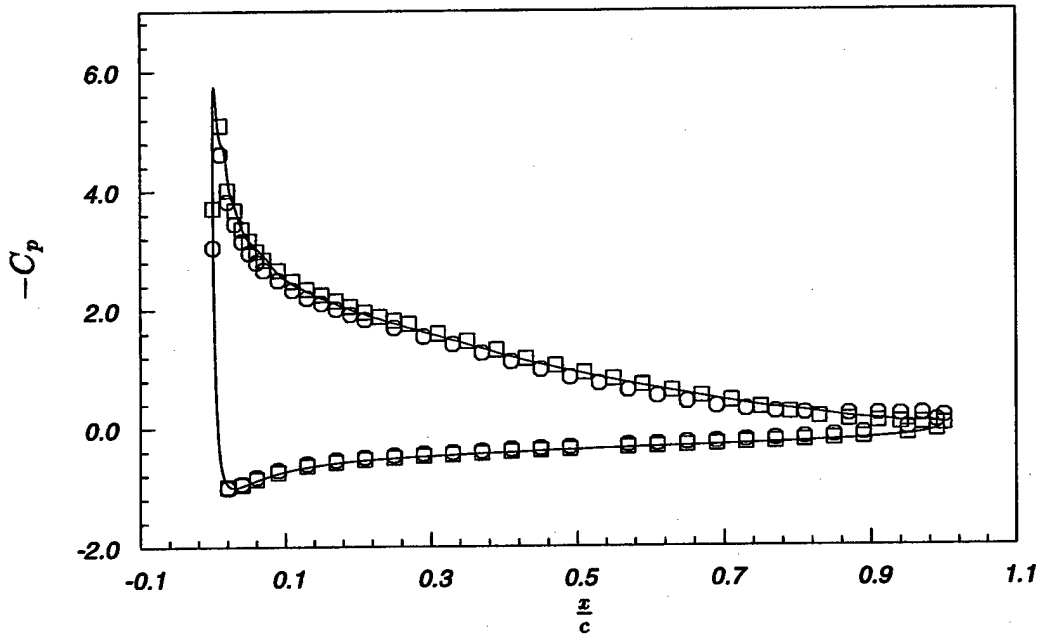


FIGURE 3. Coefficient of pressure along the airfoil surface. LES —, Hastings and Williams without trip \square , Hastings and Williams tripped \circ .

2.2.3 Grid refinement study of the nose

The dramatic change of the flow with changed resolution indicated a need for further refinement in the nose region. At the same time we also hoped to model the transition through a steady blowing pattern as shown in Fig. 4. A shape that could be easily resolved was chosen. Therefore, we could be certain that any sensitivity to grid refinement would be associated with the turbulence structures responding to the blowing and not the resolution of the blowing itself.

A new mesh was generated where the streamwise and spanwise resolution were improved by a factor of two everywhere on the upper surface. The normal spacing was improved at the wall by a factor of two as well, but this did not lead to a doubling of points in this direction due to the stretching. The spanwise domain was cut in half (from $0.05c$ to $0.025c$) for this simulation. Therefore, the number of points approximately doubled rather than a quadrupling.

There was again a rather dramatic change in the solution and so another mesh was generated. This mesh again improved the streamwise and spanwise resolution by a factor of two, although, this time, only in the first 5 percent of chord. The three surface meshes of the first 10 percent of chord are shown in Fig. 5. The velocity profiles in the first 5 percent of chord are shown in Fig. 6. For this forcing pattern, the flow is nearly spanwise- and streamwise-resolution independent.

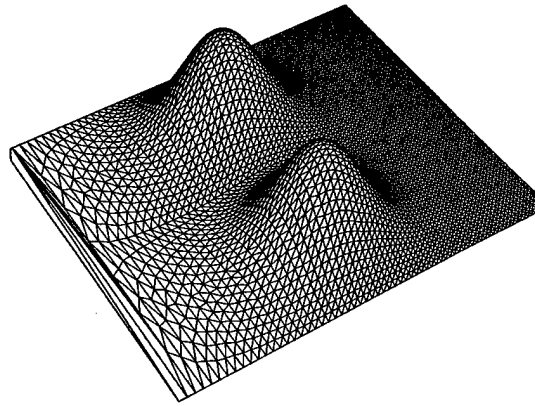


FIGURE 4. Elevation plot of the steady jet normal to the airfoil surface. The actual grid is shown to confirm resolution.

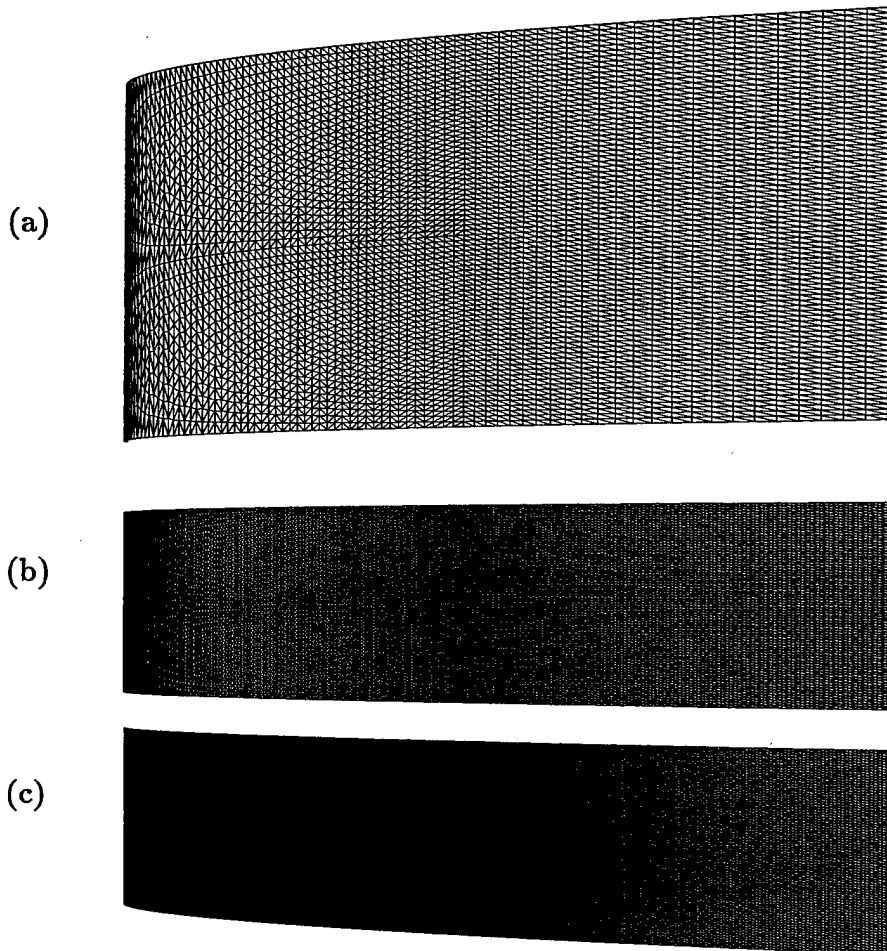


FIGURE 5. Surface meshes near the leading edge ($0.0 < x/c < 0.1$). Mesh (b) has been refined by a factor of 2, both spanwise and streamwise, from mesh (a). The spanwise domain is also halved. Mesh (c) has been refined by a factor of 2, both spanwise and streamwise, from mesh (b) in the first 5 percent of chord.

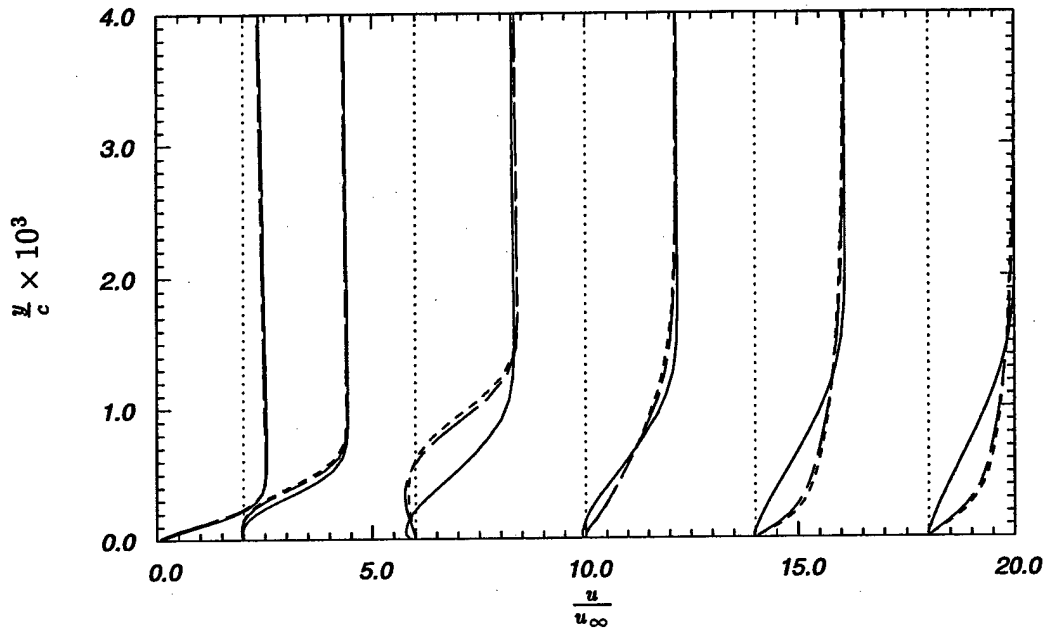


FIGURE 6. Profiles of tangential velocity component at various positions along the airfoil surface ($x/c = 0.005, 0.01, 0.02, 0.03, 0.04, 0.05$). Solutions correspond to grids from previous figure; mesh (a) —, mesh (b) ---, mesh (c) - - - .

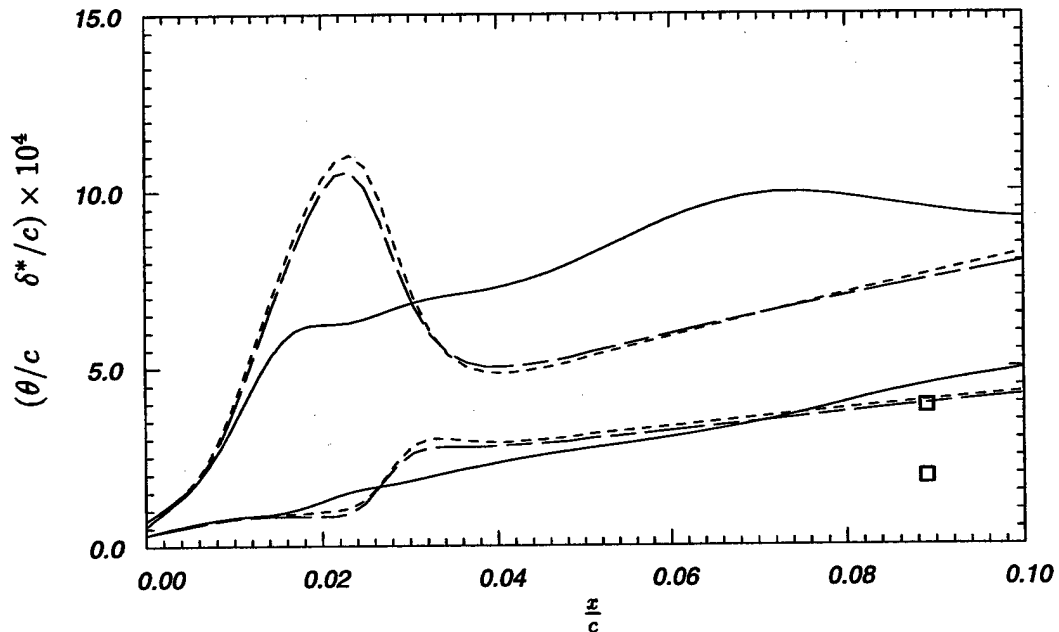


FIGURE 7. Boundary layer parameters (lower curves and data are momentum thickness (θ), higher curves and data are displacement thickness (δ^*)) along the airfoil surface. Solutions correspond to meshes from Fig. 5; mesh (a) —, mesh (b) ---, mesh (c) - - - , Wadcock (1987) (\square).

2.3 More accurate transition

While it was useful to obtain a grid-independent solution at the forcing prescribed, the final solution does not agree with experiment, as can be seen in Fig. 7. Here, the momentum and displacement thickness of the grid-independent calculations can be seen to be substantially greater than the experiments at the first available datum point. The discrepancy seems to be associated with the laminar separation at 1 percent of chord. The simulation suggests a transition in the free shear layer, followed by a turbulent reattachment. This mode of transition seems to give the flow a large jump in momentum and displacement thickness. The experiment did not seem take this route to transition. For this reason a more careful study of transition is currently underway.

Wadcock used a strip of tape with serrations cut into the edge on the upstream side. The serrated tape can be modeled in a coarse fashion by our current simulation as can be seen in Fig. 8. The tape is effectively a forward facing step (with serrations) of height $\delta_{99}/4$, followed by a backward facing step. Calculations are underway with this modification.

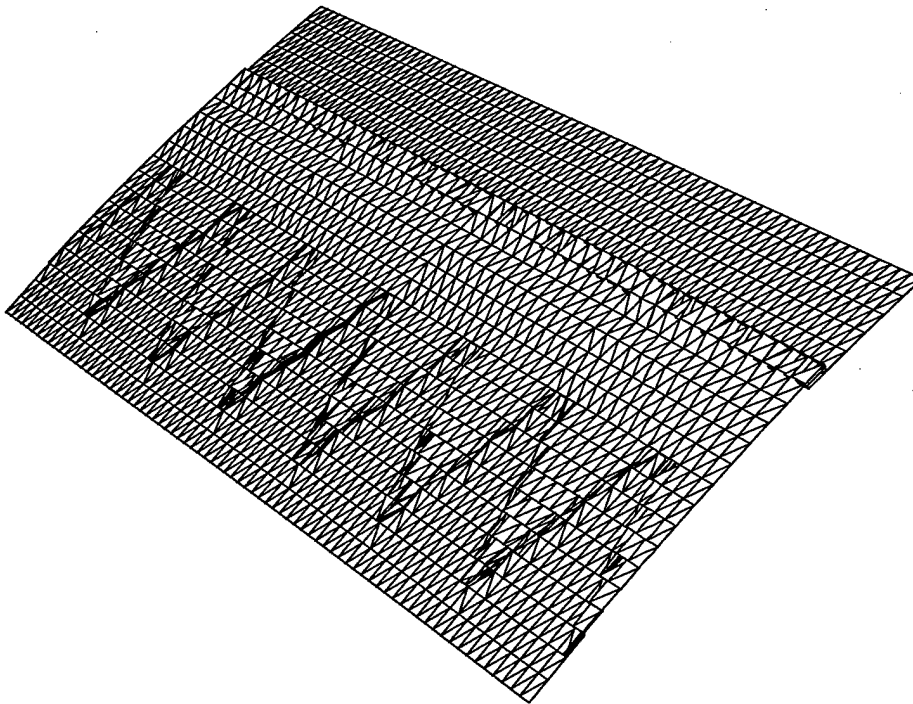


FIGURE 8. A transition strip is modeled geometrically by applying a no-slip boundary condition to the nodes which form a surface of height, shape, and position equivalent to Wadcock's serrated tape which was applied to the airfoil surface.

2.4 Reynolds-averaged simulations

Reynolds-averaged Navier-Stokes simulations (RANS) have not shown good agreement with the experimental data. However, given the cost of LES, they can be a

helpful tool for suggesting sensitivity to changes of basic flow parameters since they require so little computational time. While the results are not expected to be quantitatively correct, trends can at least be suggested by RANS and later confirmed by LES.

A series of RANS calculations was performed to chart various trends in this flow. The RANS calculations used the commonly accepted NASA code (INS2D) of Rogers (1991) and employed a $k - \omega$ model from Menter (1994). First, the effect of angle-of-attack and wind tunnel walls are compared in Figures 9 and 10. The boundary condition on the wind tunnel walls is a slip condition. This accounts for the blockage of the walls without requiring resolution of the boundary layers on them. The effects are compared together because it is common among the RANS modeling community to adjust the angle-of-attack of free air calculations to account for the walls. Figure 10 suggests that the flattening of the C_p near the trailing edge (which is associated with the large separation there) is affected strongly by angle-of-attack and only weakly by the wind tunnel walls. The 13.87° angle-of-attack cannot be justified with the hope of accounting for the effects of the wind tunnel walls in free air calculations.

The second trend studied with the RANS code was the effect of transition position. When the RANS code was run with the transition point fixed at the position of Wadcock's strip, a leading edge separation developed on sufficiently fine meshes. Once beyond the transition point, the flow reattaches. This provides an independent verification of the results observed in the LES.

3. Future plans

3.1 Grid-independent solution of flow with a transition strip

The calculation using the transition strip described above will be continued and checked for grid dependence. It should be noted that grid independence can only be achieved beyond a short distance downstream of the transition strip. True grid independence of the strip and transition itself is probably too expensive to be practical, even with an unstructured grid. It may be necessary to provide small disturbances upstream of the strip to mimic the interaction of freestream turbulence with the strip. This capability has been implemented and tested in the code using a wall jet with spatial and temporal variation.

3.2 Inclusion of the wind tunnel walls

The RANS studies indicated a moderate effect of the wind tunnel walls on the solution. Future simulations will be done with a slip boundary conditions on the wind tunnel walls. Meshes have already been generated for this purpose as can be seen in Fig. 11.

3.3 Higher order methods

Given the number of points that are required to get a grid-independent solution, it seems clear that higher order methods should be explored. This is relatively easy, but non-trivial, to do with the finite element method. There are two benefits to higher order methods besides the obvious one of higher accuracy. First, the higher

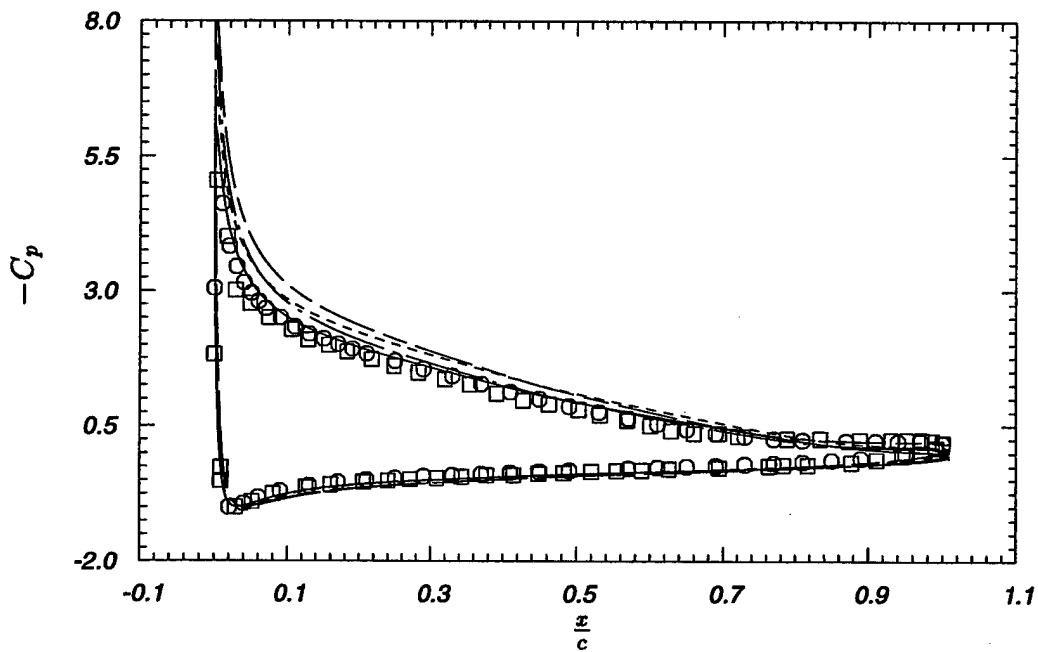


FIGURE 9. Coefficient of pressure along the airfoil surface from RANS simulations. 12° in free air —, 12° with walls ----, 13.87° in free air —·—, 13.87° with walls ———, Hastings and Williams (1987) \circ , Wadcock (1987) \square .

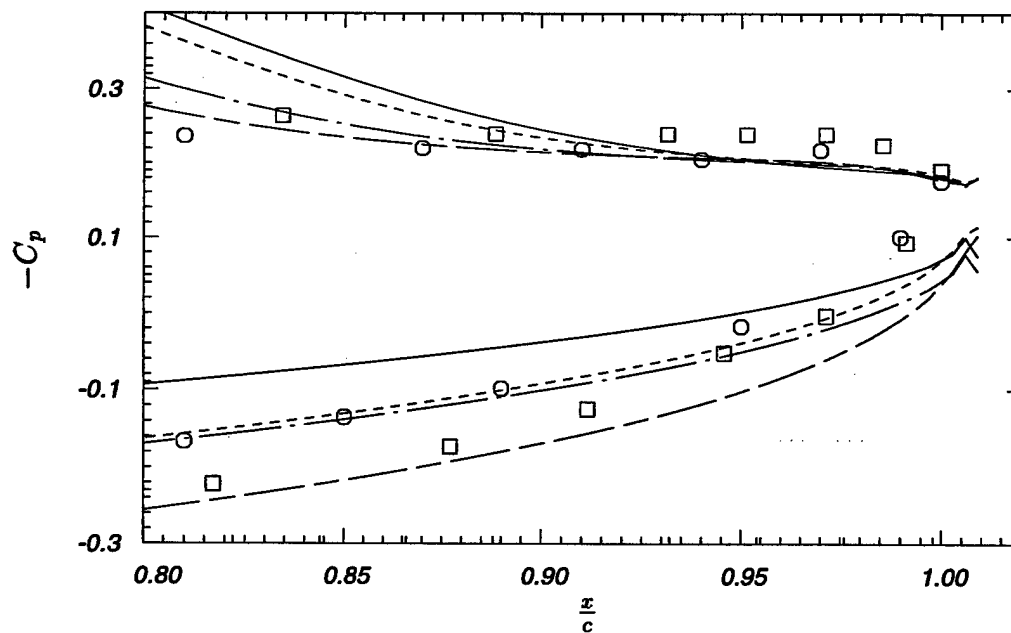


FIGURE 10. Closeup of the trailing-edge region (same legend as above).

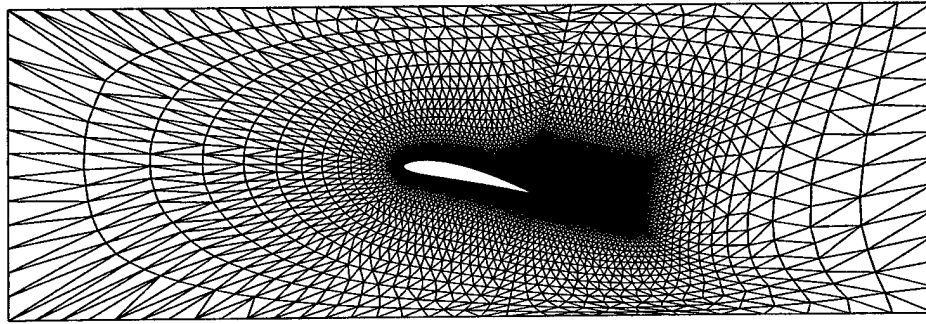


FIGURE 11. The crosssectional plane of an unstructured mesh which accounts for the inviscid effects of the wind tunnel walls.

order methods will have a more complete representation of the residual error of the discrete approximation and, therefore, the scheme will be less dissipative. Second, alternative filters, described in Jansen (1994), can be implemented and tested. It is difficult to predict at this time if the method will lose computational efficiency when extended to higher order.

3.4 Expanded spanwise domain

Once we are satisfied with the solution in the region of the nose, we will have to consider carefully the effect of the narrow spanwise domain on our solution. It is likely that as we predict a larger separation at the trailing edge, the effect of the narrow domain will become more acute. Strategies are being developed to expand only the portion of the domain suffering from a narrow box. If these strategies work a large number of points can be saved.

REFERENCES

- CHAPMAN, D. R. 1979 Computational aerodynamics development and outlook. *AIAA J.* **17**, 1293.
- COLES, D., & WADCOCK, A. J. 1979 A flying-hot-wire study of two-dimensional mean flow past an NACA 4412 airfoil at maximum lift. *AIAA J.* **17**, 321.
- HASTINGS, R. C. & WILLIAMS, B. R. 1987 Studies of the flow field near a NACA 4412 aerofoil at nearly maximum lift. *Aero. J.* **91**, 29.
- JANSEN, K. 1994 Unstructured grid large eddy simulation of flow over an airfoil. *Annual Research Briefs 1994*. Center for Turbulence Research, NASA Ames/Stanford Univ.
- JANSEN, K., JOHAN, Z., & HUGHES, T. J. R. 1993 Implementation of a one-equation turbulence model within a stabilized finite element formulation of a symmetric advective-diffusive system. *Comp Meth Appl Mech Eng.* **105**, 405.
- JOHAN, Z., HUGHES, T. J. R., MATHUR, K. K., & JOHNSON, S. L. 1992 A data parallel finite element method for computational fluid dynamics on the Connection Machine system. *Comp. Meth. Appl. Mech. Eng.* **99**, 113.

- MENTER, F. R. 1994 Two-equation eddy-viscosity turbulence models for engineering applications. *AIAA J.* **32-8**, 1598-1605.
- ROGERS, S. E., & KWAK, D. 1991 An upwind differencing scheme for the steady-state incompressible Navier-Stokes equations. *J. Appl. Num. Math.* **8**, 43-64.
- WADCOCK, A. J. 1987 Investigation of low-speed turbulent separated flow around airfoils. *NACA CR 177450*.

APPENDIX 2. Large-eddy simulation of flow around an airfoil on a structured mesh

By Hans-Jakob Kaltenbach AND Haecheon Choi

1. Motivation and objectives

The diversity of flow characteristics encountered in a flow over an airfoil near maximum lift taxes the presently available statistical turbulence models. This work describes our first attempt to apply the technique of large-eddy simulation to a flow of aeronautical interest. The challenge for this simulation comes from the high Reynolds number of the flow as well as the variety of flow regimes encountered, including a thin laminar boundary layer at the nose, transition, boundary layer growth under adverse pressure gradient, incipient separation near the trailing edge, and merging of two shear layers at the trailing edge.

The flow configuration chosen is a NACA 4412 airfoil near maximum lift. The corresponding angle of attack was determined independently by Wadcock (1987) and Hastings & Williams (1984, 1987) to be close to 12° . The simulation matches the chord Reynolds number $U_\infty c / \nu = 1.64 \times 10^6$ of Wadcock's experiment.

2. Accomplishments

2.1 Numerical method and SGS model

The numerical method for solving the unsteady, incompressible Navier-Stokes equations is described in Choi *et al.* (1993). Second-order spatial central differences on a staggered mesh are combined with a semi-implicit time integration scheme. Formulation of the problem in terms of contravariant velocity components, weighted with the Jacobian, in conjunction with the staggered variable configuration leads to discretized equations that can be solved with the classical splitting approach. The resulting pressure Poisson equation is solved using FFT for the spanwise (periodic) direction and iterative methods for the remaining two-dimensional problems. The computational cost is about equally distributed between computation of the right-hand side and solving the Poisson equation at every substep of a third order Runge Kutta time integration.

The implementation of the dynamic subgrid-scale model (Germano *et al.* 1991) with least-square contraction (Lilly 1992) uses the spanwise homogeneity of the flow to obtain a model coefficient that is a function of streamwise and wall-normal coordinate only. We found that the dynamic procedure occasionally renders unrealistic negative coefficients in regions where the flow is laminar such as at the nose or in the potential flow region. In these regions, the negative values are the result of the dynamic model becoming ill-conditioned and have no physical significance. In the present simulations we prevented any form of backscatter by constraining the model coefficient to be always positive.

x/c	δ_{99}/c	$\Delta x/c$	Δx^+	Δz^+	$\Delta x/\Delta z$	δ_{99}/L_z
0.1	0.004	0.0031	405	137	2.96	0.08
0.2	0.006	0.0033	378	118	3.2	0.12
0.4	0.016	0.0033	274	86	3.2	0.32
0.6	0.030	0.0050	235	49	4.8	0.6
0.8	0.060	0.0088	110	13	8.5	1.2

Table 1. Spacing along upper surface of airfoil. The last two columns show cell aspect ratio and ratio of boundary layer thickness to domain width for case A.

On the present mesh, the CFL limit of 1.5 results in an average timestep of $2 \times 10^{-4} c/U_\infty$. About 80 CPU-seconds on a Cray-C90 are needed to advance the solution over one timestep on a mesh of $638 \times 79 \times 48 = 2.4 \times 10^6$ cells. Therefore, simulation of one time unit c/U_∞ requires 90 CPU-hours. In order to obtain smooth statistics the results have to be averaged over several time units.

2.2 Computational domain and mesh layout

The computational domain is a C-mesh with the outer boundary about three chord lengths away from the surface. At the outer boundary we specify the freestream velocity U_∞ . As a consequence, the vertical velocity component (in a coordinate system aligned with the chord at 0° angle of attack) will be zero at the outer boundary. Therefore, the chosen configuration resembles more the flow around an airfoil inside of a wind tunnel with parallel walls than an airfoil in free air. Jansen (1995) has shown that, even with the walls located much closer, the presence of wind tunnel walls mainly affects the flow in the nose region by increasing the suction peak. The pressure distribution in the rear part and the size of the backflow zone, however, are only weakly dependent on whether the wind tunnel walls are included or not. A no-slip condition is enforced at the airfoil surface, and we use a convective (radiative) boundary condition at the outflow plane.

Results from two simulations will be presented. The two cases differ only with respect to the spanwise domain width which is $0.05c$ in case A and $0.025c$ in case B. The spanwise spacing Δz is the same with 48 cells in case A and 24 cells in case B, respectively. Main criterion for the choice of the spanwise domain size is the ratio of boundary layer thickness to domain width, which is tabulated in Table 1. As a consequence of the rapid growth of the boundary layer thickness on the suction side, this ratio, which is initially sufficiently small to capture several structures in the spanwise direction, exceeds one near the trailing edge. It is likely that the development of flow structures in the outer part of the boundary layer will be affected by the limited domain size. Comparison of cases A and B gives insight in the sensitivity of the simulation with respect to this parameter.

The design of an adequate mesh involves several aspects. The most energetic eddies of the boundary layer have to be resolved. More or less general criteria have been developed for the mesh spacing in the case of wall bounded shear flows under zero pressure gradient. However, these criteria depend on the numerical method employed (Lund *et al.*, 1995). Cabot (1994) found that for LES of turbulent channel flow based on second-order finite differences a spacing of $\Delta x^+ = 60$ and

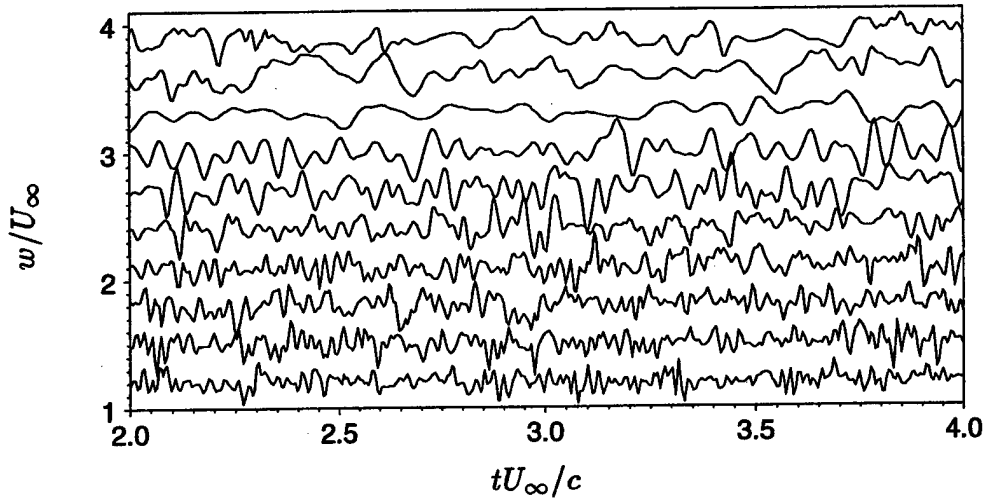


FIGURE 1. Time series of spanwise velocity fluctuation between stations $x/c = 0.24$ (bottom) and $x/c = 0.98$ (top) at about 5% of the local boundary layer height. Individual curves are separated by a vertical offset of 0.3 with the corresponding zero-lines located at 1.2, 1.5, ... 3.9.

$\Delta z^+ = 15 - 20$ is needed to adequately resolve the near wall structures.

Little is known about the minimum spacing requirements for boundary layers which are close to separation. The mesh size in terms of wall units probably becomes less relevant in this case. About half of the 640 streamwise points were distributed over the upper surface, which guaranteed that the streamwise spacing was between $1/3$ and $1/5$ of the local boundary layer thickness for most of the upper surface, see Table 1. The streamwise spacing varies considerably along the surface due to the boundary layer growth. Near the trailing edge, the grid was refined in x in order to resolve the merging of the two shear layers. No attempt was made to resolve the turbulence on the lower side of the airfoil. Spacings in terms of wall units based on the local skin friction as given in Wadcock's experiment are given in Table 1. It is evident that the spacing in the present simulation is considerably coarser than what has been found to be necessary for channel flow simulations. However, as the boundary layer develops along the surface, the resolution criteria become less restrictive so that the flow in the rear part is much better resolved than in the front section.

In the wall-normal direction we used a hyperbolic mesh generator (Chan, 1993) to distribute 79 layers of cells. The first line away from the wall was at about $y^+ = 1$, and over most of the surface there were between 20 and 30 points inside the boundary layer.

2.3 Difficulties arising from the high Reynolds number

Centered difference schemes suffer from the emergence of grid-to-grid oscillations (2- Δ -waves, wiggles) when used for high Reynolds number simulations. Usually, the viscosity provided by the subgrid-scale model is sufficient to dampen these grid-to-grid oscillations. Several sources for 2- Δ -waves have been identified in the past (Gresho, 1981). They include high cell Peclet numbers in conjunction with large

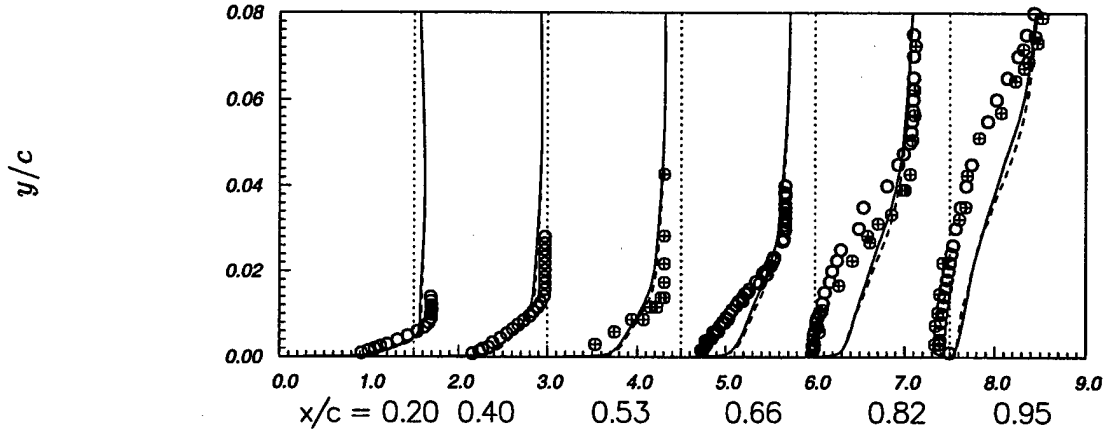


FIGURE 2. Mean velocity profiles, normalized by U_∞ , along upper surface. Symbols: case A —, B ----, measurements by Hastings \circ and Wadcock $+$.

streamwise gradients of the advected variable. This situation is typically encountered near the nose and the trailing edge of the airfoil. Other sources are the outflow boundary (an artificial boundary layer is generated in the streamwise direction) and mesh stretching. As shown by Cain & Bush (1994), waves propagating into an increasingly coarse (fine) mesh are amplified (dampened) in a centered scheme. In our simulation we find that strong 2- Δ -waves appear near the nose and near the trailing edge. The wiggles appear almost exclusively in the streamwise coordinate direction. Part of these waves travel with different phase speed and cancellation occurs. However, other parts are steady and accumulate in time. These standing waves contaminate the potential flow region after long integration times. It is difficult to assess to what degree the solution is contaminated by the presence of 2- Δ -waves. On a staggered mesh, velocity components are averaged in order to obtain fluxes at cell faces. This averaging on a scale of the mesh cell can sometimes completely hide the 2- Δ -wave. For example, the convective term $\partial(uu)/\partial x$ in the streamwise momentum balance is evaluated as

$$\frac{1}{\Delta x} \left[\left(\frac{u_{i+1} + u_i}{2} \right)^2 - \left(\frac{u_i + u_{i-1}}{2} \right)^2 \right].$$

The finite difference expression renders the same value independently whether an oscillatory part in the i -direction $\tilde{u}_i = (-1)^i u_a$ with zero mean and arbitrary amplitude u_a is added or not. Similarly, if a 2- Δ -wave in the i -direction is present in the v velocity component, it will not appear in the discrete approximation for $\partial(uv)/\partial y$. However, it will contaminate the term $\partial(uv)/\partial x$. Time averaged fields of velocity components show 2- Δ -waves in the potential flow region, but the pressure field is virtually free of wiggles. This indicates that the presence of 2- Δ -waves in the potential flow region may be tolerated to a certain degree since wiggle free streamlines in accordance with the pressure field can be reconstructed.

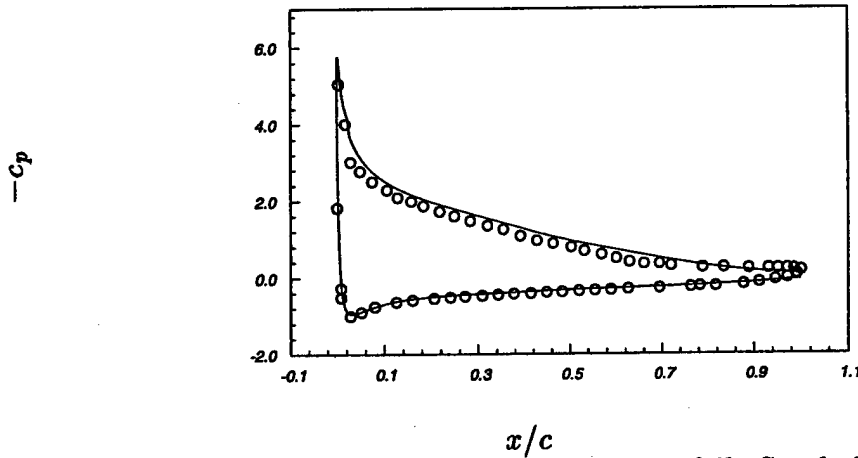


FIGURE 3. Pressure distribution around the airfoil. Symbols: LES —, Wadcock o.

The strongest effect of 2- Δ -waves comes from the associated limitations for the computational timestep. Large amplitude wiggles in the wall normal velocity component in conjunction with rather fine wallnormal spacing cause high CFL numbers near the nose. The resulting timestep limitations are so severe that the simulation can not be carried out at an affordable cost. We therefore resorted to an *ad hoc* modification of the numerical scheme. In a small region near the nose (less than 2% of the chord) we applied a 1:2:1-filter in the streamwise and spanwise direction which efficiently eliminates all 2- Δ -waves. Filtering is equivalent to adding a direction dependent diffusion term to the equations. Justification for this procedure comes from the fact that the flow near the nose is laminar and filtering on a scale of the grid cell does not affect the flow physics. Additionally, the boundary layer in the experiments was tripped at a location around $x/c = 0.02$, thereby fixing the region of laminar-turbulent transition. We find that the flow spontaneously transitions as soon as the filter ends. In this sense, we control the location of transition by setting the streamwise extent of the region where the solution is filtered. The filter extended about 40 layers away from the wall and faded to zero over another 15 layers. Unfortunately, this procedure changes the potential flow significantly. Because the mesh cells are rather large in the outer part of the domain, filtering on the grid scale is no longer negligible on the scale where the potential flow changes near the nose. Future simulations can easily avoid this problem by limiting the filter to the vicinity of the surface, i.e. it should end near the boundary layer edge. No attempt was made to dampen 2- Δ -waves in the trailing edge region where the flow is fully turbulent. Any filtering there would probably affect the flow physics.

2.4 Simulation results and discussion

Figure 1 shows time series of the spanwise velocity fluctuation w recorded at several stations along the upper surface of the airfoil. We observe a shift in the frequency which corresponds to the most energetic motions towards lower values as the recording station moves closer to the trailing edge. This is consistent with the

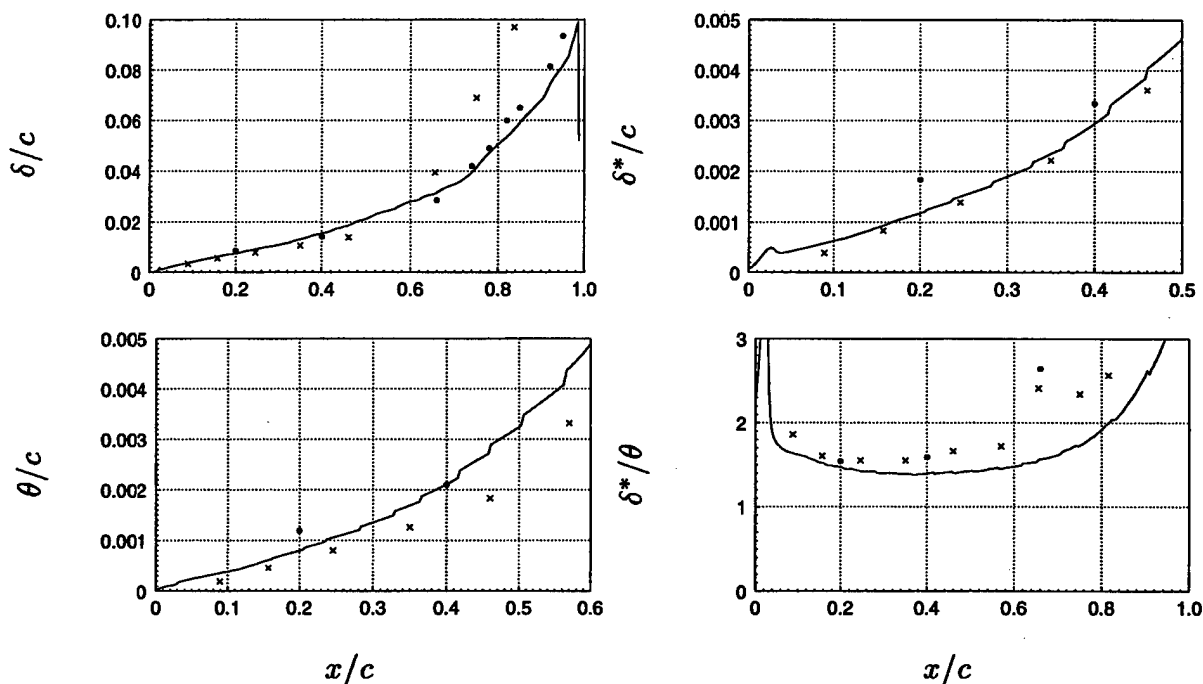


FIGURE 4. Boundary layer thickness δ , displacement thickness δ^* , momentum thickness θ and shape factor $H = \delta^*/\theta$ along the upper surface of the airfoil. Symbols: — LES, • Hastings, × Wadcock.

increase of an inertial timescale (ratio of the boundary layer thickness to the edge velocity) as the boundary layer grows under the influence of the adverse pressure gradient. It becomes evident that the solution has to be sampled over several time units c/U_∞ in order to obtain representative turbulence statistics for the rear part of the airfoil.

Statistics were obtained by averaging the instantaneous flow fields in the spanwise homogeneous direction and in time over more than $2c/U_\infty$. Profiles of the mean velocity in a surface normal coordinate system are shown in Fig. 2. At the first two stations, the edge velocity is about 12% smaller than measured by Hastings. As mentioned earlier, this is a side effect from the filter which was applied in the nose region in order to eliminate 2- Δ -waves. Since filtering was limited to a region close to the surface, simulated and measured mean flow agree much better for distances greater than $y/c = 0.06$. Although a better match between simulated and measured edge velocity is desirable (and can easily be obtained by further reducing the distance from the surface over which the filter is applied), we don't expect turbulence statistics to be significantly affected. One reason is the observation that the simulated adverse pressure gradient matches the measured one over most of the upper surface, see Fig. 3. Filtering affects mainly the magnitude of the suction peak and is partially responsible for the offset in the simulated pressure distribution. Additionally, since wind tunnel walls were not properly considered in this simulation, the pressure distribution near the nose will deviate from the measured one, see Jansen (1995). The goal of the present study is to predict the boundary layer growth and

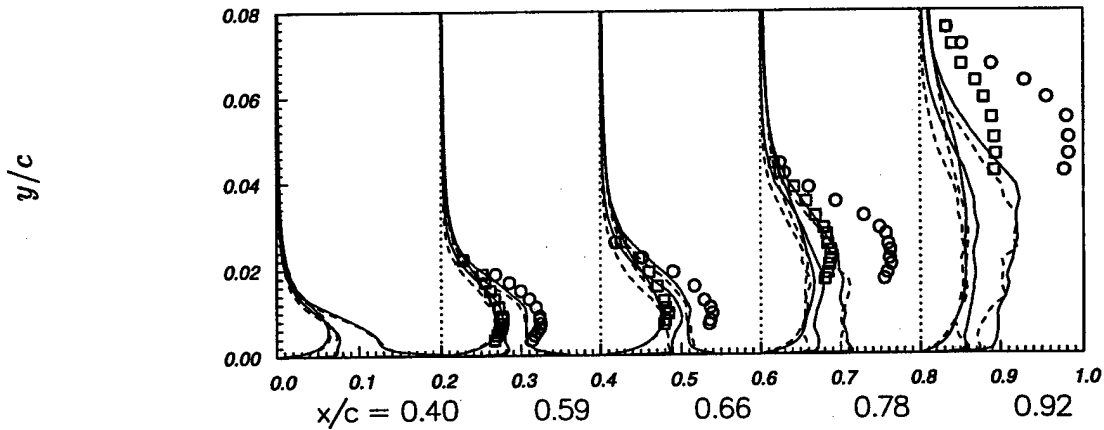


FIGURE 5. RMS of velocity fluctuations u' , v' and w' , normalized with U_∞ . Symbols: case A —, B ----, u' \circ and v' \square from Hastings. In terms of relative magnitude, the three curves for each simulation are v' , w' , and u' respectively.

the amount of separation near the trailing edge. Accurate prediction of the suction peak is of secondary interest.

Displacement and momentum thickness from the simulation lie in between the measurements of Hastings & Williams (1984) and Wadcock (1987) upstream of $x/c = 0.4$, see Fig. 4. The experimental values differ by up to 40% as a result of differences in boundary layer tripping and Reynolds number. However, the measured shape factor $H \approx 1.55$ is similar in both experiments in the region $x/c = 0.2 \dots 0.4$. Contrary to the experiment, H drops gradually in the simulation in the region $x/c = 0.2 \dots 0.4$ and reaches values as low as 1.4.

Since both experiments measure similar boundary layer growth and flow retardation near the trailing edge, the flow development does not seem to be very sensitive with respect to the exact values of δ^* and θ of the turbulent boundary that develops behind the transition strip. Although the thickness of the simulated boundary layer is close to the measured ones in the front part of the airfoil, the underprediction of the shape factor in the simulation and the initially opposite trend (decline as opposed to a growth) indicates insufficiencies in the simulated boundary layer for a considerable part of the upper surface. This is not surprising since the resolution is so coarse that the near wall structures can hardly be resolved properly. Examination of instantaneous flow fields close to the surface reveals a very streaky structure with typical spacings in the order of a few mesh cells. Similarly, spanwise two point correlations show a zero-crossing within 2-3 spanwise grid points for all near-wall locations upstream of $x/c = 0.5$, see Fig. 6. This indicates that the simulation has marginal resolution near the wall. Further evidence comes from the comparison of the present case with an earlier simulation which was a factor of 2 coarser in the streamwise direction and a factor of 1.5 coarser in the spanwise direction. The flow

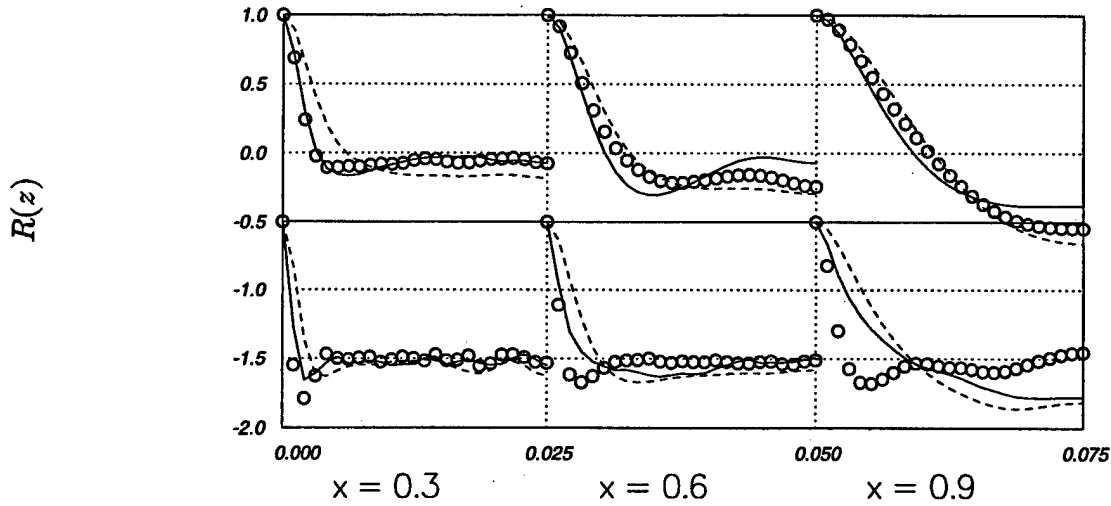


FIGURE 6. Spanwise two-point correlations R_{uu} (—), R_{vv} (o) and R_{ww} (----) versus distance z/c for three stations along the upper surface. Bottom figures correspond to the near wall region, top figures to $y/\delta \approx 0.3$. The y coordinate of the lower figures is shifted, i.e. $y = -1.5$ corresponds to a zero correlation.

retardation and the boundary layer growth was significantly improved on the finer mesh. Therefore, further grid refinement and, subsequently, a better prediction of the boundary layer in the front region might lead to better agreement between simulation and measurements over the entire airfoil.

The shear stress provided by the SGS model is an indicator for the role of the SGS model. The maximum contribution is about 15% of the resolved stress \overline{uv} and is found in the front part of the airfoil where the resolution is coarse. Near the trailing edge, the SGS stress is negligible compared to the resolved Reynolds shear stress. The ratio of SGS eddy viscosity to molecular viscosity is about 20, which emphasizes the important role of the model for the kinetic energy budget.

RMS values of the velocity fluctuations are shown in Fig. 5. Agreement between simulation and experiment is reasonable in the middle section of the airfoil. In a characteristic manner for an adverse pressure gradient boundary layer, the location of maximum rms values (and Reynolds shear stress) moves towards the outer part of the boundary layer. Also, the anisotropy of the fluctuations in the outer part of the boundary layer is greatly reduced. Substantial differences between simulation and experiment are indicated by the large discrepancy in simulated and measured rms values (and shear stress) near the trailing edge. It is unclear whether this mismatch is a local effect or rather a result of differences in (spatial) flow history between experiment and simulation.

Results from cases A and B, which only differ with respect to the spanwise domain size, are surprisingly similar. Two-point correlations from the outer part of the boundary layer of case A do not drop to zero within half the spanwise width for locations downstream of $x/c = 0.6$, see Fig. 6. This means that the large scales

of motion are affected by the presence of artificial periodic boundaries. Since the limitations are much more severe in case B as compared to A, one would expect that both cases deviate in the rear part. Presently, it is not clear why the simulation is rather insensitive with regard to the domain width. Kaltenbach (1994) made a similar observation for a flow in a diffuser where the aspect ratio of the outlet duct was smaller than 0.5. Doubling the aspect ratio had only a small effect on the flow evolution. The cost for case B is about half that of case A. Further studies on the effect of grid refinement would be much cheaper if the domain width of case B turns out to be sufficient.

3. Conclusions and future goals

Wall resolving LES of flow around an airfoil has been demonstrated to be feasible with present computers and standard numerical schemes for LES. Qualitatively, the simulation captures typical features of separating flows such as boundary layer retardation and drastic increase in Reynolds stresses. This demonstrates the capability of the LES concept to deal with flows in complex configurations of immediate technical interest. However, the resolution provided was probably too coarse to adequately simulate the boundary layer in the first half of the airfoil. Although the resolution might have been adequate for the rear part, the overall agreement with measurements with respect to prediction of backflow is not satisfactory. History effects might play a role, and further studies should attempt to match better the integral boundary layer parameters of the experiment at an early station. Because of conservation properties, the use of centered difference schemes is very desirable in the context of LES. However, the emergence of 2- Δ -waves is a serious problem for the present high Reynolds number flow and needs further consideration, for example, usage of explicit filters as explored by Lund & Kaltenbach in this volume. Comparison of two cases with different domain width did not show significant sensitivity with respect to this parameter in the range considered. Future simulations should consider the effect of wind tunnel (top and bottom) walls by a corresponding modification of domain size and boundary conditions.

REFERENCES

- CABOT, W. 1994 Local dynamic subgrid-scale models in channel flow. In *Annual Research Briefs 1994*, Center for Turbulence Research, Stanford Univ./NASA Ames Research Center, 143-159.
- CAIN, A. B. & BUSH, R. H. 1994 Numerical wave propagation analysis for stretched grids. *AIAA-94-0172*, 32nd Aerospace sciences meeting, Jan. 10-13, 1994, Reno, NV.
- CHAN, W. M. 1993 User's Manual for the HYPGEN hyperbolic grid generator. *NASA Technical Memorandum 108791*.
- CHOI, H., MOIN, P. & KIM, J. 1993 Direct numerical simulation of turbulent flow over riblets. *J. Fluid Mech.* **255**, 503-539.

- GERMANO, M., PIOMELLI, U., MOIN, P. & CABOT, W. H. 1991 A dynamic subgrid-scale eddy viscosity model. *Phys. Fluids A*. **3**, 1760-1765.
- GRESHO, P. M. & LEE, R. L. 1981 Don't suppress wiggles - they're telling you something. *Computers & Fluids*. **9**, 223-253.
- HASTINGS, R. C. & WILLIAMS, B. R. 1984 Studies of the flow field near an NACA 4412 aerofoil at nearly maximum lift. *Royal Aircraft Establishment, Technical Memorandum Aero 2026*.
- HASTINGS, R. C. & WILLIAMS, B. R. 1987 Studies of the flow field near an NACA 4412 aerofoil at nearly maximum lift. *Aeronautical Journal*. **91**, 29-44.
- JANSEN, K. 1995 Preliminary large-eddy simulations of flow around a NACA 4412 airfoil using unstructured grids. *Article in this volume*.
- KALTENBACH, H.-J. 1994 Large eddy simulation of flow through a plane, asymmetric diffuser. In *Annual Research Briefs 1994*, Center for Turbulence Research, Stanford Univ./NASA Ames Research Center, 175-184.
- LILLY, D. K. 1992 A proposed modification of the Germano subgrid scale closure method. *Phys. Fluids A*. **3**, 2746-2757.
- LUND, T. S., KALTENBACH, H.-J. & AKSELVOLL, K. 1995 On the behavior of centered finite difference schemes for large eddy simulation. In *Proceedings of the sixth International Symposium on Computational Fluid Dynamics*, Lake Tahoe, NV, 4-8 September, 1995.
- WADCOCK, A. J. 1987 Investigation of low-speed turbulent separated flow around airfoils. *NASA contractor report 177450*.

APPENDIX 3. Conservative properties of finite difference schemes for incompressible flow

By Youhei Morinishi¹

1. Motivation and objectives

The purpose of this research is to construct accurate finite difference schemes for incompressible unsteady flow simulations such as LES (large-eddy simulation) or DNS (direct numerical simulation).

Experience has shown that kinetic energy conservation of the convective terms is required for stable incompressible unsteady flow simulations. Arakawa (1966) showed that a finite difference scheme that conserves the enstrophy in the absence of viscous dissipation is required for long-time integration in the two-dimensional vorticity-streamfunction formulation. The corresponding conserved variable is kinetic energy in velocity-pressure formulation, and some energy conservative finite difference schemes have been developed for the Navier-Stokes equations in three dimensions. Staggered grid systems are usually required to obtain physically correct pressure fields. The standard second order accurate finite difference scheme (Harlow & Welch 1965) in a staggered grid system conserves kinetic energy and this scheme has proven useful for LES and DNS. However, the accuracy of the second order finite difference scheme is low and fine meshes are required (Ghosal 1995). Spectral methods (Canuto *et al.* 1988) offer supreme accuracy, but these methods are limited to simple flow geometries. Existing fourth order accurate convective schemes (A-Domis 1981, Kajishima 1994) for staggered grid systems do not conserve kinetic energy. Higher order staggered grid schemes that conserve kinetic energy have not been presented in the literature.

The conservation of kinetic energy is a consequence of the Navier-Stokes equations for incompressible flow in the inviscid limit. In contrast, energy conservation in a discrete sense is not a consequence of momentum and mass conservation. It is possible to derive numerical schemes that conserve both mass and momentum but do not conserve kinetic energy. It is also possible to derive schemes that conserve kinetic energy even though mass or momentum conservation are violated.

In this report, conservation properties of the continuity, momentum, and kinetic energy equations for incompressible flow are specified as analytical requirements for a proper set of discretized equations. Existing finite difference schemes in staggered grid systems are checked for satisfaction of the requirements. Proper higher order accurate finite difference schemes in a staggered grid system are then proposed. Plane channel flow is simulated using the proposed fourth order accurate finite difference scheme and the results compared with those of the second order accurate Harlow and Welch (1965) algorithm.

1 Permanent address: Nagoya Institute of Technology, Japan

2. Accomplishments

2.1 Analytical requirements

The continuity and momentum equations describe the motion of incompressible flow. For convenience later in the analysis, these equations are written symbolically as

$$(Cont.) = 0 \quad (1)$$

$$\frac{\partial v_i}{\partial t} + (Conv.)_i + (Pres.)_i + (Visc.)_i = 0 \quad (2)$$

where

$$(Cont.) \equiv \frac{\partial v_i}{\partial x_i}, \quad (Pres.)_i \equiv \frac{\partial p}{\partial x_i}, \quad (Visc.)_i \equiv \frac{\partial \tau_{ij}}{\partial x_j} \quad (3), (4), (5)$$

Here, v_i is velocity component, p is pressure divided by density, and τ_{ij} is viscous stress. Henceforth, p will be referred to as pressure.

The conservation properties of Eqs. (1) and (2) will now be established. Note that Eq. (2) is in the following form.

$$\frac{\partial \phi}{\partial t} + {}^1 Q^\phi + {}^2 Q^\phi + {}^3 Q^\phi + \dots = 0 \quad (6)$$

The term ${}^k Q^\phi$ is *conservative* if it can be written in divergence form

$${}^k Q^\phi = \nabla \cdot ({}^k F_j^\phi) = \frac{\partial ({}^k F_j^\phi)}{\partial x_j} \quad (7)$$

To see that the divergence form is conservative, integrate Eq. (6) over the volume and make use of Gauss's theorem for the flux terms $k = 1, 2, \dots$, all of which are assumed to satisfy Eq. (7)

$$\frac{\partial}{\partial t} \int \int \int_V \phi \, dV = - \int \int_S ({}^1 F^\phi + {}^2 F^\phi + {}^3 F^\phi + \dots) \cdot dS \quad (8)$$

From Eq. (8), we notice that the time derivative of the sum of ϕ in a volume V equals the sum of the flux ${}^k F^\phi$ on the surface S of the volume. In particular, the sum of ϕ never changes in periodic field if ${}^k Q^\phi$ is conservative for all k .

Note that the pressure $(Pres.)_i$ and viscous terms $(Visc.)_i$ are conservative *a priori* in the momentum equation since they appear in divergence form. The convective term is also conservative *a priori* if it is cast in divergence form. This is not always the case, however, and we shall investigate alternative formulations. To perform the analysis, we regard $(Conv.)_i$ as a generic form of the convective term in the momentum equation. At least four types of convective forms have been used traditionally in analytical or numerical studies. These forms are defined as follows.

$$(Div.)_i \equiv \frac{\partial v_j v_i}{\partial x_j} \quad (9)$$

$$(Adv.)_i \equiv v_j \frac{\partial v_i}{\partial x_j} \quad (10)$$

$$(Skew.)_i \equiv \frac{1}{2} \frac{\partial v_j v_i}{\partial x_j} + \frac{1}{2} v_j \frac{\partial v_i}{\partial x_j} \quad (11)$$

$$(Rot.)_i \equiv v_j \left(\frac{\partial v_i}{\partial x_j} - \frac{\partial v_j}{\partial x_i} \right) + \frac{1}{2} \frac{\partial v_j v_j}{\partial x_i} \quad (12)$$

As mentioned above, the *divergence* form, $(Div.)$, is conservative *a priori*. $(Adv.)_i$, $(Skew.)_i$, and $(Rot.)_i$ are referred to as *advective*, *skew-symmetric*, and *rotational* forms respectively. The four forms are connected with each other through following relations.

$$(Adv.)_i = (Div.)_i - v_i \cdot (Cont.) \quad (13)$$

$$(Skew.)_i = \frac{1}{2} (Div.)_i + \frac{1}{2} (Adv.)_i \quad (14)$$

$$(Rot.)_i = (Adv.)_i \quad (15)$$

We notice that there are only two independent convective forms, and the two are equivalent if $(Cont.) = 0$ is satisfied. It is also apparent that the advective, skew-symmetric, and rotational forms are conservative as long as the continuity equation is satisfied.

The transport equation of the square of a velocity component, $v_1^2/2$, is v_1 times $i = 1$ component of Eq. (2).

$$\frac{\partial v_1^2/2}{\partial t} + v_1 \cdot (Conv.)_1 + v_1 \cdot (Pres.)_1 + v_1 \cdot (Visc.)_1 = 0 \quad (16)$$

In the above equation, the convective term can be modified into the following forms corresponding to those in the momentum equation.

$$v_1 \cdot (Div.)_1 = \frac{\partial v_j v_1^2/2}{\partial x_j} + \frac{1}{2} v_1^2 \cdot (Cont.) \quad (17)$$

$$v_1 \cdot (Adv.)_1 = \frac{\partial v_j v_1^2/2}{\partial x_j} - \frac{1}{2} v_1^2 \cdot (Cont.) \quad (18)$$

$$v_1 \cdot (Skew.)_1 = \frac{\partial v_j v_1^2/2}{\partial x_j} \quad (19)$$

Note that the skew-symmetric form is conservative *a priori* in the velocity square equation. Since the rotational form is equivalent to advective form, the four convective forms are conservative if $(Cont.) = 0$ is satisfied.

The terms involving pressure and viscous stress in Eq. (16) can be modified into following forms.

$$v_1 \cdot (Pres.)_1 = \frac{\partial p v_1}{\partial x_1} - p \frac{\partial v_1}{\partial x_1} \quad (20)$$

Terms in Momentum Eq.	Transport Equations		
	v_i	$v_1^2/2$	K
(Div.)	⊙	○	○
(Adv.) = (Rot.)	○	○	○
(Skew.)	○	⊙	⊙
(Pres.)	⊙	×	○
(Visc.)	⊙	×	×

Table 1. Conservative properties of convective, pressure, and viscous terms in the v_i , $v_1^2/2$, and K equations. ⊙ is conservative *a priori*, ○ is conservative if $(Cont.) = 0$ is satisfied, and × is not conservative.

$$v_1 \cdot (Visc.)_1 = \frac{\partial \tau_{1j} v_1}{\partial x_j} - \tau_{1j} \frac{\partial v_1}{\partial x_j} \quad (21)$$

These terms are not conservative since they involve the pressure-strain and the viscous dissipation.

We can determine the conservative properties of $v_2^2/2$ and $v_3^2/2$ in the same manner as for $v_1^2/2$.

The transport equation of kinetic energy, $K \equiv v_i v_i / 2$, is v_i times i component of Eq. (2) with summation over i .

$$\frac{\partial K}{\partial t} + v_i \cdot (Conv.)_i + v_i \cdot (Pres.)_i + v_i \cdot (Visc.)_i = 0 \quad (22)$$

In Eq. (22), the conservation property of the convective term is determined in the same manner as for $v_1^2/2$. In addition, the terms involving pressure and viscous stress in Eq. (22) can be modified into following forms.

$$v_i \cdot (Pres.)_i = \frac{\partial p v_i}{\partial x_i} - p \cdot (Cont.) \quad (23)$$

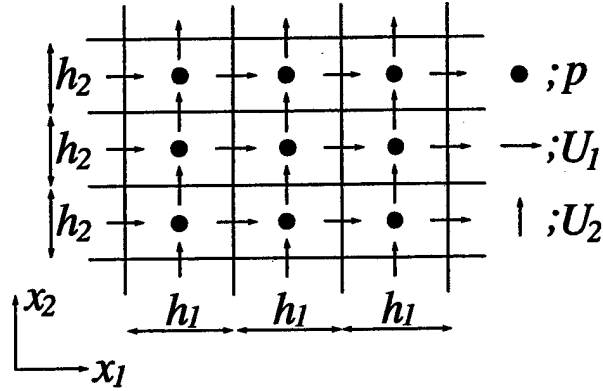
$$v_i \cdot (Visc.)_i = \frac{\partial \tau_{ij} v_i}{\partial x_j} - \tau_{ij} \frac{\partial v_i}{\partial x_j} \quad (24)$$

The pressure term in Eq. (22) is conservative if $(Cont.) = 0$ is satisfied. The viscous stress term in Eq. (22) is not conservative because the second term on the right-hand side of Eq. (24) is the energy dissipation.

Table 1 provides a summary of conservative properties of convective, pressure and viscous terms in the transport equations of v_i , $v_1^2/2$ and K for incompressible flow. The final goal of this work is to derive higher order accurate finite difference schemes that satisfy these conservative properties in a discretized sense.

2.2 Discretized operators

Before starting the main discussion, discretized operators need to be defined. In this report, the discussion of the discretized equations will be limited to uniform

FIGURE 1. Staggered grid system in $x_1 - x_2$ plane.

grid systems. The widths of the numerical grid in each direction, h_1 , h_2 , h_3 , are constant. The grid system shown in Fig. 1 will be referred to as a *staggered* grid system. In the staggered grid system, the velocity components U_i ($i = 1, 2, 3$) are distributed around the pressure points. The continuity equation is discretized centered at pressure points. The momentum equation corresponding to each velocity component is centered at the respective velocity point.

Let the finite difference operator acting on ϕ with respect to x_1 and with stencil n be defined as follows.

$$\left. \frac{\delta_n \phi}{\delta_n x_1} \right|_{x_1, x_2, x_3} \equiv \frac{\phi(x_1 + nh_1/2, x_2, x_3) - \phi(x_1 - nh_1/2, x_2, x_3)}{nh_1} \quad (25)$$

Also, define an interpolation operator acting on ϕ in the x_1 direction with stencil n as follows.

$$\left. \overline{\phi}^{nx_1} \right|_{x_1, x_2, x_3} \equiv \frac{\phi(x_1 + nh_1/2, x_2, x_3) + \phi(x_1 - nh_1/2, x_2, x_3)}{2} \quad (26)$$

In addition, define a special interpolation operator of the product between ϕ and ψ in the x_1 direction with stencil n .

$$\begin{aligned} \left. \widetilde{\phi\psi}^{nx_1} \right|_{x_1, x_2, x_3} &\equiv \frac{1}{2} \phi(x_1 + nh_1/2, x_2, x_3) \psi(x_1 - nh_1/2, x_2, x_3) \\ &\quad + \frac{1}{2} \psi(x_1 + nh_1/2, x_2, x_3) \phi(x_1 - nh_1/2, x_2, x_3) \end{aligned} \quad (27)$$

Equations (25) and (26) are second order accurate approximations to first derivative and interpolation, respectively. Combinations of the discretized operators can be used to make higher order accurate approximations to the first derivative and interpolation. For example, fourth order accurate approximations are as follows.

$$\frac{9}{8} \frac{\delta_1 \phi}{\delta_1 x_1} - \frac{1}{8} \frac{\delta_3 \phi}{\delta_3 x_1} \simeq \frac{\partial \phi}{\partial x_1} - \frac{3}{640} \frac{\partial^5 \phi}{\partial x_1^5} h_1^4 + \dots \quad (28)$$

$$\frac{9}{8}\bar{\phi}^{1x_1} - \frac{1}{8}\bar{\phi}^{3x_1} \simeq \phi - \frac{3}{128} \frac{\partial^4 \phi}{\partial x_1^4} h_1^4 + \dots \quad (29)$$

Discretized operators in the x_2 and x_3 directions are defined in the same way as for the x_1 direction.

We define two types of conservative forms in the discretized systems. ${}^k Q^\phi$ in Eq. (6) is (*locally*) *conservative* if the term can be written as

$${}^k Q^\phi = \frac{\delta_1({}^k F_j^{1\phi})}{\delta_1 x_j} + \frac{\delta_2({}^k F_j^{2\phi})}{\delta_2 x_j} + \frac{\delta_3({}^k F_j^{3\phi})}{\delta_3 x_j} + \dots \quad (30)$$

This definition corresponds to the analytical conservative form of Eq. (7). ${}^k Q^\phi$ is *globally conservative* if the following relation holds in a periodic field.

$$\sum_{x_1} \sum_{x_2} \sum_{x_3} {}^k Q^\phi \Delta V = 0 \quad (31)$$

The sum that appears in Eq. (31) is taken over the period of respective direction. $\Delta V (\equiv h_1 h_2 h_3)$ is a constant in a uniform grid system. The definition of global conservation corresponds to the conservation property of Eq. (8) in a periodic field. The condition for (local) conservation satisfies the condition for global conservation.

2.3 Continuity and pressure term in a staggered grid system

Now we are ready to consider our main problem. First of all, let's examine the conservative property of the pressure term. As we have observed, the pressure term should be conservative in the transport equations of momentum and kinetic energy.

In the staggered grid system, define the discretized continuity and pressure term as follows.

$$(Cont. - S2) \equiv \frac{\delta_1 U_i}{\delta_1 x_i} = 0 \quad (32)$$

$$(Pres. - S2)_i \equiv \frac{\delta_1 p}{\delta_1 x_i} \quad (33)$$

The $-S2$ denotes that the above approximations are second order accurate in space. Fourth order approximations for the continuity and pressure term in the staggered grid system are

$$(Cont. - S4) \equiv \frac{9}{8} \frac{\delta_1 U_i}{\delta_1 x_i} - \frac{1}{8} \frac{\delta_3 U_i}{\delta_3 x_i} = 0, \quad (34)$$

$$(Pres. - S4)_i \equiv \frac{9}{8} \frac{\delta_1 p}{\delta_1 x_i} - \frac{1}{8} \frac{\delta_3 p}{\delta_3 x_i}. \quad (35)$$

Local kinetic energy can not be defined uniquely in staggered grid systems since the velocity components are defined on staggered grid points. Some sort of interpolation must be used in order to obtain the three components of the kinetic energy at the same point. The required interpolations for the pressure terms in the v_1^2 and K equations are

$$\overline{U_i \frac{\delta_1 p}{\delta_1 x_i}}^{1x_i} = \frac{\delta_1 U_i \bar{p}^{1x_i}}{\delta_1 x_i} - p \cdot (Cont - S2), \quad (36)$$

FD Schemes for Momentum Eq.	Transport Equations		
	U_i	$U_1^2/2$	K
(Pres. - S2)	\odot	\times	\bigcirc_1
(Pres. - S4)	\odot	\times	\bigcirc_2

Table 2. Conservative properties of finite difference schemes for the pressure term in a staggered grid system. \odot is conservative *a priori*, \bigcirc_1 is globally conservative if $(Cont. - S2) = 0$ is satisfied, \bigcirc_2 is globally conservative if $(Cont. - S4) = 0$ is satisfied, and \times is not conservative.

$$\frac{9}{8} \overline{U_i \frac{\delta_1 p}{\delta_1 x_i}}^{1x_i} - \frac{1}{8} \overline{U_i \frac{\delta_3 p}{\delta_3 x_i}}^{3x_i} = \frac{9}{8} \frac{\delta_1 U_i \bar{p}^{1x_i}}{\delta_1 x_i} - \frac{1}{8} \frac{\delta_3 U_i \bar{p}^{3x_i}}{\delta_3 x_i} - p \cdot (Cont - S4). \quad (37)$$

The following relations can be used to show global conservation unambiguously.

$$\sum_{x_1} \sum_{x_2} \sum_{x_3} \overline{U_i \frac{\delta_1 p}{\delta_1 x_i}}^{1x_i} = \sum_{x_1} \sum_{x_2} \sum_{x_3} U_i \cdot (Pres. - S2)_i \quad (38)$$

$$\sum_{x_1} \sum_{x_2} \sum_{x_3} \left(\frac{9}{8} \overline{U_i \frac{\delta_1 p}{\delta_1 x_i}}^{1x_i} - \frac{1}{8} \overline{U_i \frac{\delta_3 p}{\delta_3 x_i}}^{3x_i} \right) = \sum_{x_1} \sum_{x_2} \sum_{x_3} U_i \cdot (Pres. - S4)_i \quad (39)$$

Therefore, Eqs. (33) and (35) are globally conservative if the corresponding discretized continuity equations are satisfied.

Table 2 shows the summary of the conservative property of the discretized pressure terms in a staggered grid system.

2.4 Convective schemes in a staggered grid system

As we have already mentioned, local kinetic energy $K (\equiv U_i U_i / 2)$ can not be defined uniquely in a staggered grid system. Let us assume that a term is (locally) conservative in the transport equation of K if the term is (locally) conservative in the transport equations of $U_1^2/2$, $U_2^2/2$ and $U_3^2/2$. Since the conservative properties of $U_2^2/2$ and $U_3^2/2$ are estimated in the same manner as for $U_1^2/2$, only conservative properties of convective schemes in the momentum and $U_1^2/2$ equations need to be considered.

2.4.1 Proper second order accurate convective schemes

Define second order accurate convective schemes in a staggered grid system as follows.

$$(Div. - S2)_i \equiv \frac{\delta_1 \overline{U_j}^{1x_i} \overline{U_i}^{1x_j}}{\delta_1 x_j} \quad (40)$$

$$(Adv. - S2)_i \equiv \overline{\overline{U_j}^{1x_i} \frac{\delta_1 U_i}{\delta_1 x_j}}^{1x_j} \quad (41)$$

$$(Skew. - S2)_i \equiv \frac{1}{2}(Div. - S2)_i + \frac{1}{2}(Adv. - S2)_i \quad (42)$$

FD Schemes for Momentum Eq.	Transport Equations		
	U_i	$U_i^2/2$	K
(Div. - S2)	⊙	○	○
(Adv. - S2)	○	○	○
(Skew. - S2)	○	⊙	⊙

Table 3. Conservative properties of proper second order accurate convective schemes in a staggered grid system. ⊙ is conservative *a priori* and ○ is conservative if $(Cont. - S2) = 0$ is satisfied.

$(Adv. - S2)_i$ is connected with $(Div. - S2)_i$ through the following relation.

$$(Adv. - S2)_i = (Div. - S2)_i - U_i \cdot \overline{(Cont. - S2)}^{1x_i} \quad (43)$$

$(Div. - S2)_i$ is the standard divergence form in a staggered grid system (Harlow & Welch 1965). $(Adv. - S2)_i$ was proposed by Kajishima (1994). $(Skew. - S2)_i$ is equivalent to the scheme that was proposed by Piacsek & Williams (1970). $(Div. - S2)_i$ is conservative *a priori* in the momentum equation. The product between U_1 and $(Skew. - S2)_1$ can be rewritten as

$$U_1 \cdot (Skew. - S2)_1 = \frac{\delta_1 \overline{U_j}^{1x_1} \widetilde{U_1 U_1}^{1x_j} / 2}{\delta_1 x_j}. \quad (44)$$

Therefore, $(Skew. - S2)_1$ is conservative *a priori* in the transport equation of $U_1^2/2$. By using Eq. (43), conservative properties of the various schemes are determined. Table 3 shows the conservative properties of $(Div. - S2)_i$, $(Adv. - S2)_i$ and $(Skew. - S2)_i$. These schemes are seen to be conservative provided continuity is satisfied. In addition, the rotational form is also conservative in light of Eq. (15).

2.4.2 Proposal of proper higher order accurate convective schemes

It is of interest to derive a proper fourth order accurate convective scheme for a staggered grid system. Existing fourth order accurate convective schemes for staggered grid systems (A-Domis 1981, Kajishima 1994) do not conserve kinetic energy. Here, we propose the following set of fourth order accurate convective schemes in a staggered grid system.

$$(Div. - S4)_i \equiv \frac{9}{8} \frac{\delta_1}{\delta_1 x_j} \left[\left(\frac{9}{8} \overline{U_j}^{1x_i} - \frac{1}{8} \overline{U_j}^{3x_i} \right) \overline{U_i}^{1x_j} \right] - \frac{1}{8} \frac{\delta_3}{\delta_3 x_j} \left[\left(\frac{9}{8} \overline{U_j}^{1x_i} - \frac{1}{8} \overline{U_j}^{3x_i} \right) \overline{U_i}^{3x_j} \right] \quad (45)$$

$$(Adv. - S4)_i \equiv \frac{9}{8} \overline{\left(\frac{9}{8} \overline{U_j}^{1x_i} - \frac{1}{8} \overline{U_j}^{3x_i} \right) \frac{\delta_1 U_i}{\delta_1 x_j}}^{1x_j} - \frac{1}{8} \overline{\left(\frac{9}{8} \overline{U_j}^{1x_i} - \frac{1}{8} \overline{U_j}^{3x_i} \right) \frac{\delta_3 U_i}{\delta_3 x_j}}^{3x_j} \quad (46)$$

FD Schemes for Momentum Eq.	Transport Equations		
	U_i	$U_1^2/2$	K
(Div. - S4)	\odot	\bigcirc	\bigcirc
(Adv. - S4)	\bigcirc	\bigcirc	\bigcirc
(Skew. - S4)	\bigcirc	\odot	\odot

Table 4. Conservative properties of proper fourth order accurate convective schemes in a staggered grid system. \odot is conservative *a priori* and \bigcirc is conservative if $(Cont. - S4) = 0$ is satisfied.

$$(Skew. - S4)_i \equiv \frac{1}{2}(Div. - S4)_i + \frac{1}{2}(Adv. - S4)_i \quad (47)$$

$(Div. - S4)_i$ is conservative *a priori* in the momentum equation. The product between U_1 and $(Skew. - S4)_1$ can be rewritten as follows.

$$U_1 \cdot (Skew. - S4)_1 = \frac{9}{8} \frac{\delta_1}{\delta_1 x_j} \left[\left(\frac{9}{8} \overline{U_j^{1x_1}} - \frac{1}{8} \overline{U_j^{3x_1}} \right) \frac{\widetilde{U_1 U_1^{1x_j}}}{2} \right] - \frac{1}{8} \frac{\delta_3}{\delta_3 x_j} \left[\left(\frac{9}{8} \overline{U_j^{1x_1}} - \frac{1}{8} \overline{U_j^{3x_1}} \right) \frac{\widetilde{U_1 U_1^{3x_j}}}{2} \right] \quad (48)$$

Thus, $(Skew. - S4)_i$ is conservative *a priori* in the transport equation of $U_1^2/2$. The relation between $(Adv. - S4)_i$ and $(Div. - S4)_i$ is the following.

$$(Adv. - S4)_i = (Div. - S4)_i - U_i \cdot \left[\frac{9}{8} \overline{(Cont. - S4)^{1x_i}} - \frac{1}{8} \overline{(Cont. - S4)^{3x_i}} \right] \quad (49)$$

This equation is a proper discrete analog Eq. (13), and $(Adv. - S4)_i$, $(Div. - S4)_i$, and $(Skew. - S4)_i$ are equivalent if $(Cont. - S4) = 0$ is satisfied. Using this relation, the conservative properties of the present schemes are determined. Table 4 shows the conservative properties of the present schemes. Comparing Table 4 with Table 1, we see that the present schemes are a proper set of convective schemes provided that the continuity equation is satisfied.

Proper higher order accurate finite difference schemes in a staggered grid system can be constructed in the same way as for the fourth order schemes.

2.5 Channel flow simulation

Numerical tests of the schemes described above are performed using plane channel flow. The continuity and momentum equations for incompressible viscous flow are solved using the proper second and fourth order accurate finite difference schemes in a staggered grid system using the dynamic subgrid scale model (Germano *et al.* 1991). The flow is driven by a streamwise pressure gradient. A semi-implicit time marching algorithm is used where the diffusion terms in the wall normal direction

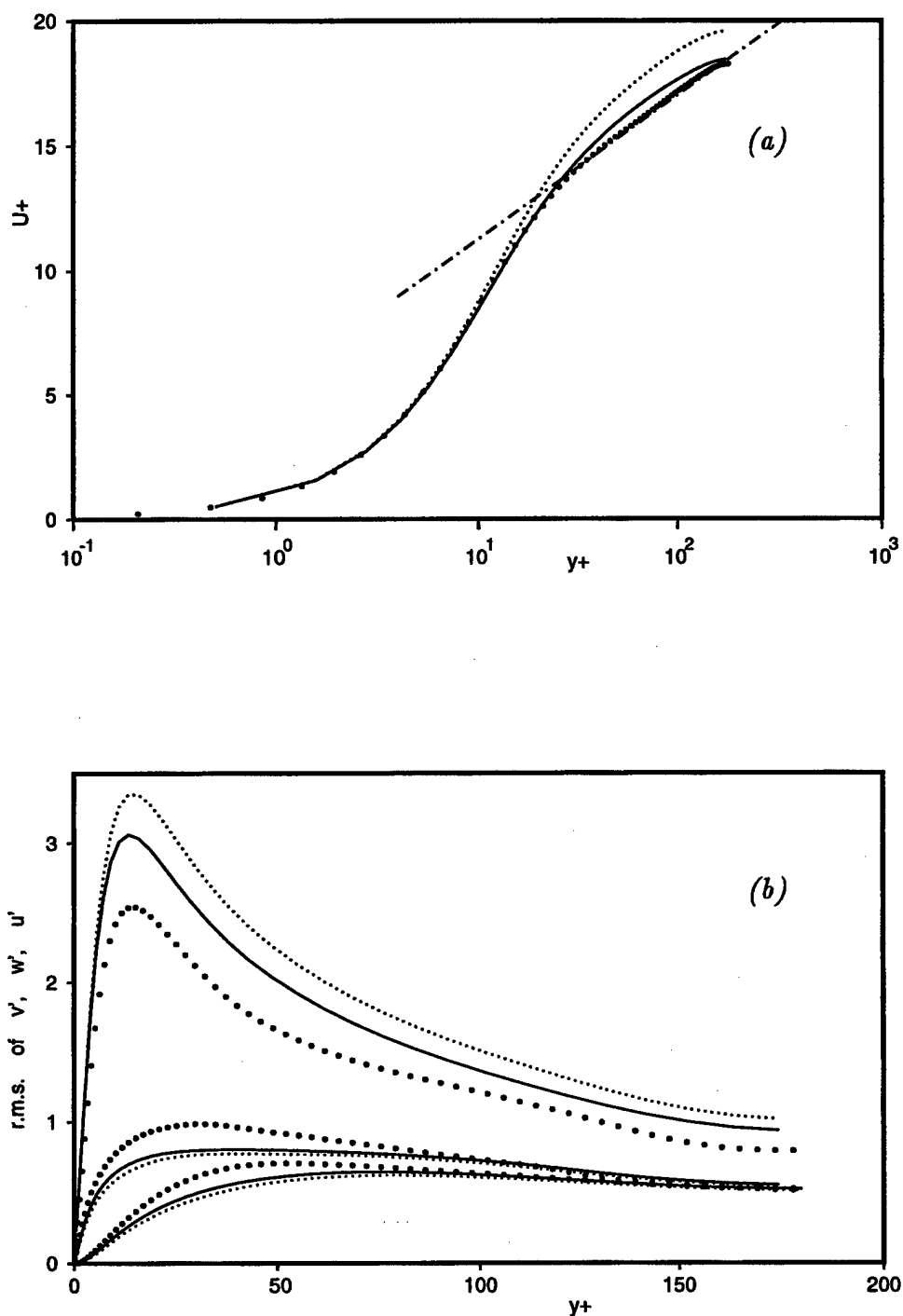


FIGURE 2. LES of plane channel flow at $Re=180$ by proper second and fourth order accurate finite difference. (a) Mean streamwise velocity; (b) Velocity fluctuations. Symbols: : 2nd order scheme; — : 4th order scheme; • : DNS, Kim, *et al.* (1987); — — ; $U^+ = 5.5 = 2.5 \log y^+$.

are treated implicitly with the Crank-Nicolson scheme and a third order Runge-Kutta scheme (Wray 1986) is used for all other terms. The fractional step method (Dukowicz & Dvinsky 1992) is used in conjunction with the Van Kan (1986) type of pressure term and wall boundary treatment. Periodic boundary conditions are imposed in the streamwise and spanwise directions.

The subgrid-scale model is the dynamic model (Germano *et al.* 1991) with the least square technique (Lilly 1992). Averaging in homogeneous directions is used. Filtering is performed in the spanwise and streamwise directions.

The spatial discretization of the second order scheme is a usual one: (*Div.* - $S2$) for the convective term, (*Pres.* - $S2$) for the pressure term, and (*Cont.* - $S2$) for the continuity. The corresponding Poisson's equation of pressure is solved using a tri-diagonal matrix algorithm in wall normal direction with fast Fourier transforms (FFT) in the periodic directions. The second order accurate control volume type discretization is used for the viscous term.

The spacial discretization of the fourth order scheme is as follows. The convective term, the pressure term, and the continuity are discretized by (*Div.* - $S4$), (*Pres.* - $S4$), and (*Cont.* - $S4$), respectively. The corresponding Poisson's equation of pressure is solved using a septa-diagonal matrix algorithm in wall normal direction with FFT in the periodic directions. A fourth order accurate control volume type discretization is used for the viscous term. The subgrid scale terms are estimated with second order finite differences. The wall boundary condition of the fourth order scheme is designed to conserve mass and momentum in the wall normal direction in a discretized sense.

The Reynolds number based on channel half width and wall friction velocity, Re , is 180. The computational box is $4\pi \times 2 \times \frac{4}{3}\pi$, and the mesh contains $32 \times 65 \times 32$ points (streamwise, wall-normal, and spanwise respectively).

Figure 2 shows the profiles of mean streamwise velocity and velocity fluctuations from the proper second and fourth order schemes. Filtered DNS data (Kim *et al.* 1987) are plotted as a reference in the figures. The mean streamwise velocity profile from the second order scheme is shifted up in the logarithmic region. This defect of the second order scheme is usually observed in coarse LES (Cabot 1994). Another defect of the second order scheme in coarse LES is the peak value of streamwise velocity fluctuation is too high (Cabot 1994). These defects are improved by using the fourth order scheme. The computational cost of the fourth order method is about 1.9 times that for the second order method.

3. Future plans

The fourth order scheme will be tested in high Reynolds number channel flow to see if it has a greater advantage when the velocity fluctuations have a relatively larger fraction of energy near the cutoff wavenumber.

Acknowledgments

The author would like to thank Dr. T. Lund for helpful comments and for checking the manuscript. I would especially like to thank Dr. H. Kaltenbach for

his helpful suggestions. I would also like to thank Prof. P. Moin for inviting me to CTR, Dr. K. Jansen for his helpful comments, Dr. W. Cabot for use of his data base, and Ms. D. Spinks for her warm hospitality at CTR. In addition, I was supported financially by the Japanese Government Research Fellowship funds for the period while at CTR.

REFERENCES

- A-DOMIS, M. 1981 Large-eddy simulation of a passive scalar in isotropic turbulence. *J. Fluid Mech.* **104**, 55.
- ARAKAWA, A. 1966 Computational design for long-term numerical integration of the equations of fluid motion: Two-dimensional incompressible flow. Part I. *J. Comp. Phys.* **1**, 119.
- CABOT, W. 1994 Local dynamic subgrid-scale models in channel flow. *Annual Research Briefs 1994*, Center for Turbulence Research, Stanford Univ./NASA Ames Research Center. 143.
- CANUTO, C., HUSSAINI, M. Y., QUARTERONI, A., & ZANG, S. A. 1988 *Spectral Methods in Fluid Dynamics*. Springer-Verlag.
- DUKOWICZ, J. K., & DVINSKY, A. S. 1992 Approximation as a high order splitting for the implicit incompressible flow equations. *J. Comp. Phys.* **102**, 336.
- GERMANO, M., PIOMELLI, U., MOIN, P., & CABOT, W. H. 1991 A dynamic subgrid-scale eddy viscosity model. *Phys. Fluids A*. **3**, 1760.
- GHOSAL, S. 1995 Analysis of discretization errors in LES (*in this briefs*).
- KAJISHIMA, T. 1994 Conservation properties of finite difference method for convection (*in Japanese*). *Trans. of JSME*. **60-574B**, 2058.
- KIM, J., & MOIN, P. 1985 Application of a fractional step method to incompressible Navier-Stokes equations. *J. Comp. Phys.* **59**, 308.
- KIM, J., MOIN, P., & MOSER, R. 1987 Turbulence statistics in fully developed channel flow at low Reynolds number. *J. Fluid Mech.* **177**, 133.
- LILLY, D. 1992 A proposed modification of the Germano subgrid-scale closure method. *Phys. Fluids A*. **4**, 633.
- HARLOW, F. H., & WELCH, J. E. 1965 Numerical calculation of time-dependent viscous incompressible flow of fluid with free surface. *Phys. of Fluids*. **8**, 2182.
- PIACSEK, S. A., & WILLIAMS, G. P. 1970 Conservation properties of convection difference schemes. *J. Comp. Phys.* **6**, 392.
- VAN KAN, J. 1986 A second-order accurate pressure-correction scheme for viscous incompressible flow. *SIAM J. Sci. Stat. Comp.* **7**(3), 870.
- WRAY, A. A. 1986 NASA-Ames Research Center, Moffett Field, CA, Private communication.

APPENDIX 4. Large-eddy simulation of flow around a NACA 4412 airfoil using unstructured grids

By Kenneth Jansen¹

1. Motivation and objectives

Large-eddy simulation (LES) has matured to the point where application to complex flows is desirable. The extension to higher Reynolds numbers leads to an impractical number of grid points with existing structured-grid methods. Furthermore, most real world flows are rather difficult to represent geometrically with structured grids. Unstructured-grid methods offer a release from both of these constraints. However, just as it took many years for structured-grid methods to be well understood and reliable tools for LES, unstructured-grid methods must be carefully studied before we can expect them to attain their full potential.

In the past three years, important building blocks have been put into place, making possible a careful study of LES on unstructured grids. The first building block was an efficient mesh generator which allowed the placement of points according to smooth variation of physical length scales. This variation of length scales is in all three directions independently, which allows a large reduction in points when compared to structured-grid methods, which can only vary length scales in one direction at a time. The second building block was the development of a dynamic model appropriate for unstructured grids. The principle obstacle was the development of an unstructured-grid filtering operator. New filtering operators were developed in Jansen (1994). In the past year, some of these filters have been implemented into a highly parallelized finite element code based on the Galerkin/least-squares finite element method (see Jansen *et al.* 1993 and Johan *et al.* 1992).

We have chosen the NACA 4412 airfoil at maximum lift as the first simulation for a variety of reasons. First, it is a problem of significant interest since it would be the first LES of an aircraft component. Second, this flow has been the subject of three experimental studies (Coles and Wadcock 1979, Hasting and Williams 1987, and Wadcock 1987). The first study found the maximum lift angle to be 13.87° . The later studies found the angle to be 12° . Wadcock reports in the later study that the early data agree very well with his new data at 12° , suggesting that the early experiment suffered from a non-parallel mean flow in the Caltech wind tunnel. It should be pointed out that the Reynolds-averaged simulations are usually run at 13.87° and do not agree with the data when run at 12° as was shown in Jansen (1995). It is hoped that LES can clarify this controversy. The third reason for considering this flow is the variety of flow features which provide an important test

¹ Present address: Rensselaer Polytechnic Institute, Troy, NY

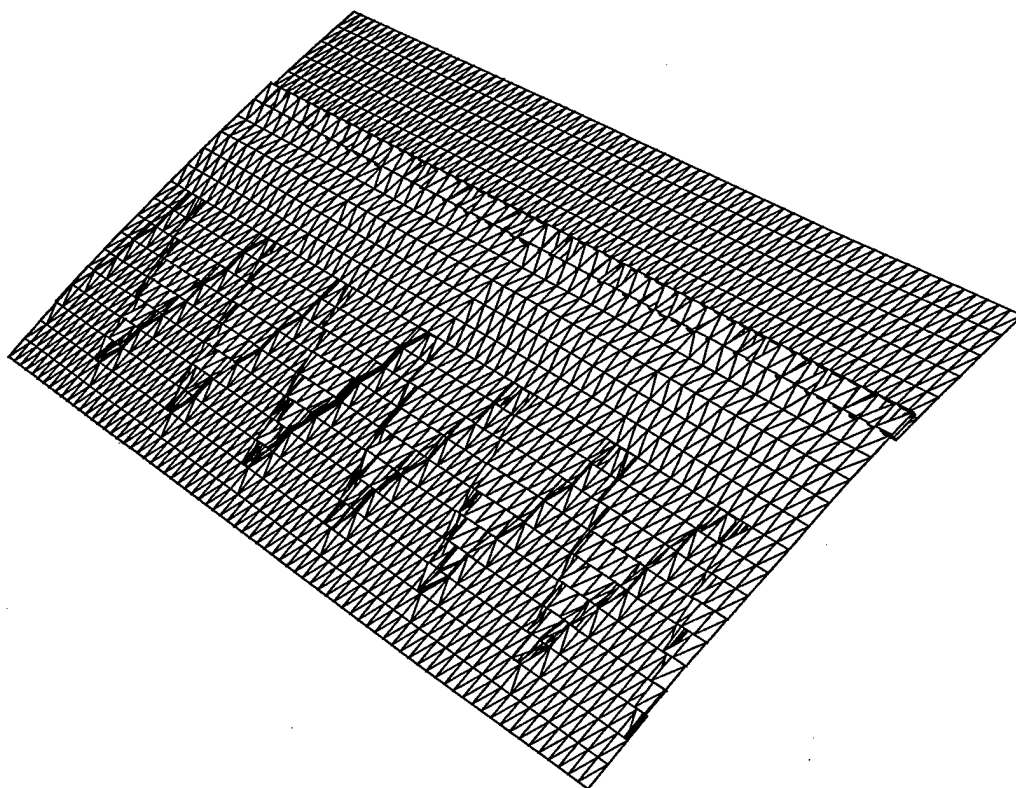


FIGURE 1. A transition strip is modeled geometrically by applying a no-slip boundary condition to the nodes which form a surface of height, shape, and position equivalent to Wadcock's serrated tape which was applied to the airfoil surface.

of the dynamic model. Starting from the nose where the flow stagnates, thin laminar boundary layers are formed in a very favorable pressure gradient. This pressure gradient soon turns adverse, driving the flow toward a leading edge separation. Only the onset of turbulence can cause the flow to remain attached or to reattach if it did separate. The persistent adverse pressure gradient eventually drives the turbulent flow to separate in the last 20 percent of chord. The separation bubble is closed near the trailing edge as the retarded upper surface boundary layer interacts with the very thin lower surface boundary layer. The large difference in boundary layers creates a challenging wake to simulate. Only the dynamic model can be expected to perform satisfactorily in this variety of situations: from the laminar regions where it must not modify the flow at all to the turbulent boundary layers and wake where it must represent a wide variety of subgrid-scale structures.

The flow configuration we have chosen is that of Wadcock (1987) at Reynolds number based on chord $Re_c = u_\infty c / \nu = 1.64 \times 10^6$, Mach number $M = 0.2$, and 12° angle of attack.

2. Accomplishments

2.1 Effect of wind tunnel walls and transition strip

In Jansen (1995) a grid independent solution was obtained which did not agree well with the experiments in the separated region. This was not completely surprising since two important effects of the experiment were not accounted for in the simulation: the wind tunnel walls and the transition strip.

Wadcock used a strip of tape with serrations cut into the edge on the upstream side. The serrated tape has been modeled in a coarse fashion by our current simulation as can be seen in Fig. 1. The tape is effectively a forward facing step (with serrations) of height $\delta_{99}/4$, followed by a backward facing step.

The blockage effect of the wind tunnel walls has also been included in the recent calculations. Note that the boundary layers on the walls are not simulated; rather, slip boundary conditions are applied on the wind tunnel walls as can be seen in Fig. 2.

These two effects were studied separately for a short period of time (not sufficient for converged statistics in the trailing edge region) and agreement with experiments was seen to improve in both cases. The effect of the walls was somewhat greater than that of the transition strip. This discussion is left qualitative because the enormous cost of these calculations led us to abandon the individual effect studies in favor of using our limited resources on converging the combined effect simulation. The results of this simulation can be seen in Fig. 3 where the velocity profiles of the new simulation (with wind tunnel walls and transition strip) are compared to the original simulation. Note the large increase in the degree of separation.

Though the new simulation is in better agreement with the experiment, new problems were created. As can be seen in Fig. 4, there is a reduction in the three-dimensionality of the turbulence in the separated region. A similar story is told by the two-point correlation in this region, which shows very little decay. While some reduction is to be expected, concern developed as to whether the periodic boundary condition, which is applied in the spanwise direction, was promoting spanwise coherent vortices due to insufficient spanwise extent. From Fig. 3 it is apparent that the boundary layer is significantly thicker in the new simulation. With a spanwise domain width, W of 2.5% of chord the spanwise domain becomes less than a boundary layer height at about two-thirds of the chord length.

2.2 Wider domain simulation

The most obvious choice of doubling the domain while maintaining the current resolution was postponed in lieu of a doubling of the domain by doubling the spanwise size of each element. The rationale for this decision was that the refinement studies of Jansen (1995) showed only a small change from the current grid to the twice coarser grid. The new simulation would also not engender an increased cost since the number of nodes remained the same. It was assumed that changes in the first half of the airfoil would suggest inadequate resolution while changes in the trailing edge region would address the domain width question.

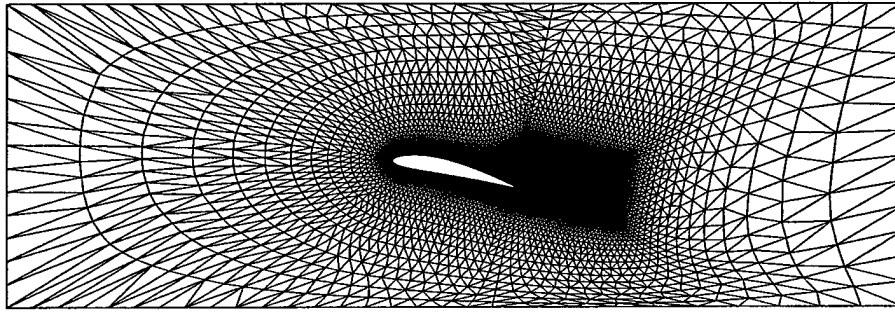


FIGURE 2. The cross sectional plane of an unstructured mesh which accounts for the inviscid effects of the wind tunnel walls.

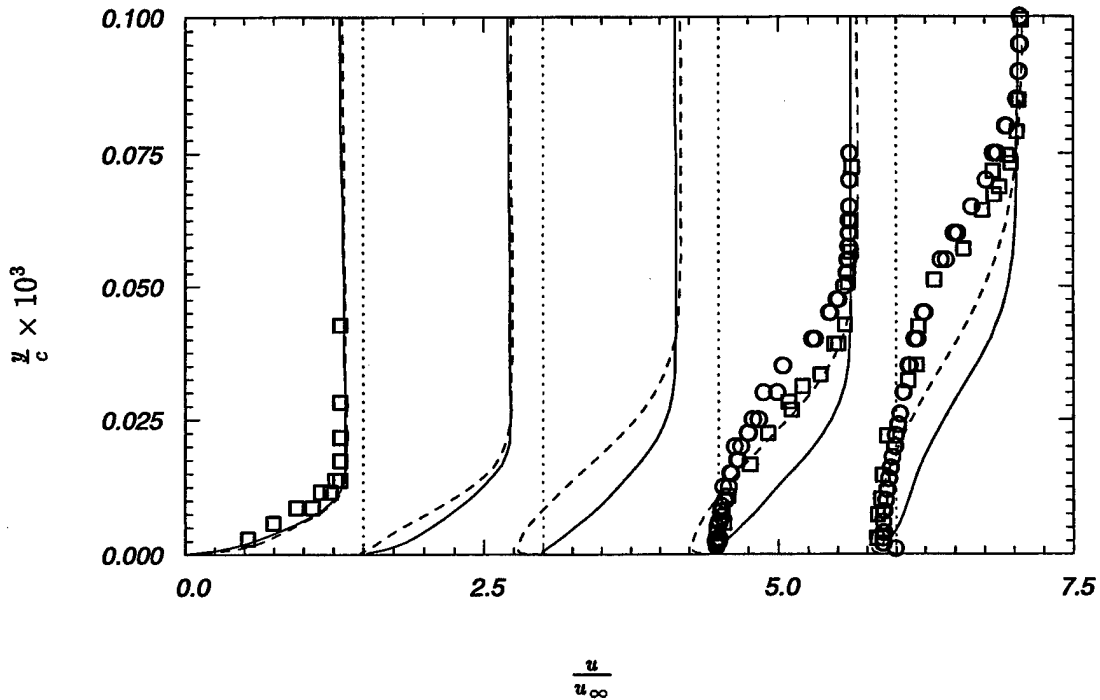


FIGURE 3. Profiles of tangential velocity component at various positions along the airfoil surface ($x/c = 0.59, 0.66, 0.78, 0.82, 0.95$). Solutions correspond to: without wind tunnel walls or transition strip —, with wind tunnel walls and transition strip ----, Wadcock \square , Hastings and Williams \circ .

The times-series from the new simulation are presented in Fig. 5 where the three-dimensionality can be seen to return to the separated region. The amount of separation is reduced, causing some departure from the experimental data as can be seen in Fig. 6. This is to be expected because the presence of three-dimensional vortical structures in the separated region pump high momentum fluid down to the

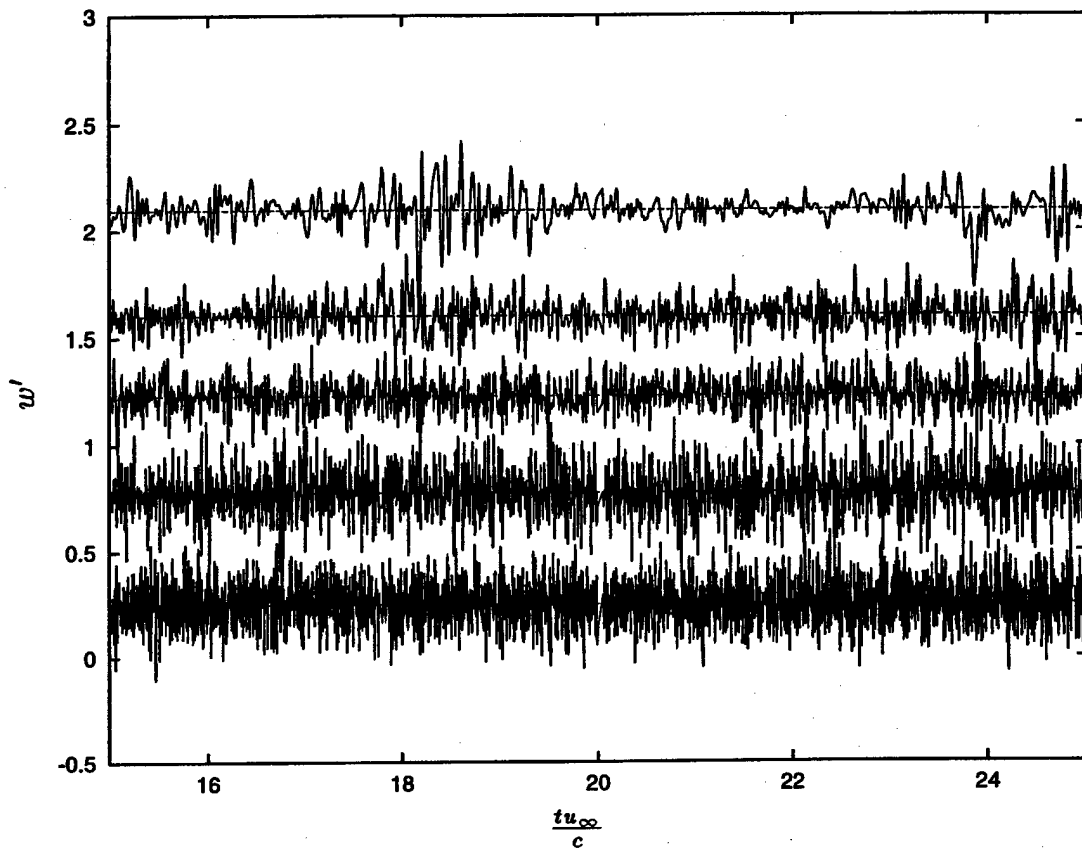


FIGURE 4. Time series of the spanwise velocity fluctuation at various positions along the chord length, approximately half a boundary layer height off of the wall. From the bottom up ($x/c = 0.1, 0.3, 0.529, 0.66, 0.815, 0.95$). Note that the top curve ($x/c = 0.95$) indicates a loss of three-dimensionality in the separated region.

wall, reducing the magnitude of the separation. Fig. 6 also illustrates that the first half of the airfoil is nearly grid independent.

3. Future plans

3.1 More spanwise domain studies

Based on the findings in the previous section more attention will be given to the spanwise domain effects. Since the resolution changed at the same time as the expansion of the domain, it is difficult to isolate the two effects. For this reason the first study will maintain the 5% chord domain width and improve the resolution in the second half of the airfoil where the solution has shown some change. A grid has already been generated to accomplish this task, and a simulation has just begun. The number of nodes has gone up by 70%, making this simulation significantly more expensive than the others described in this report.

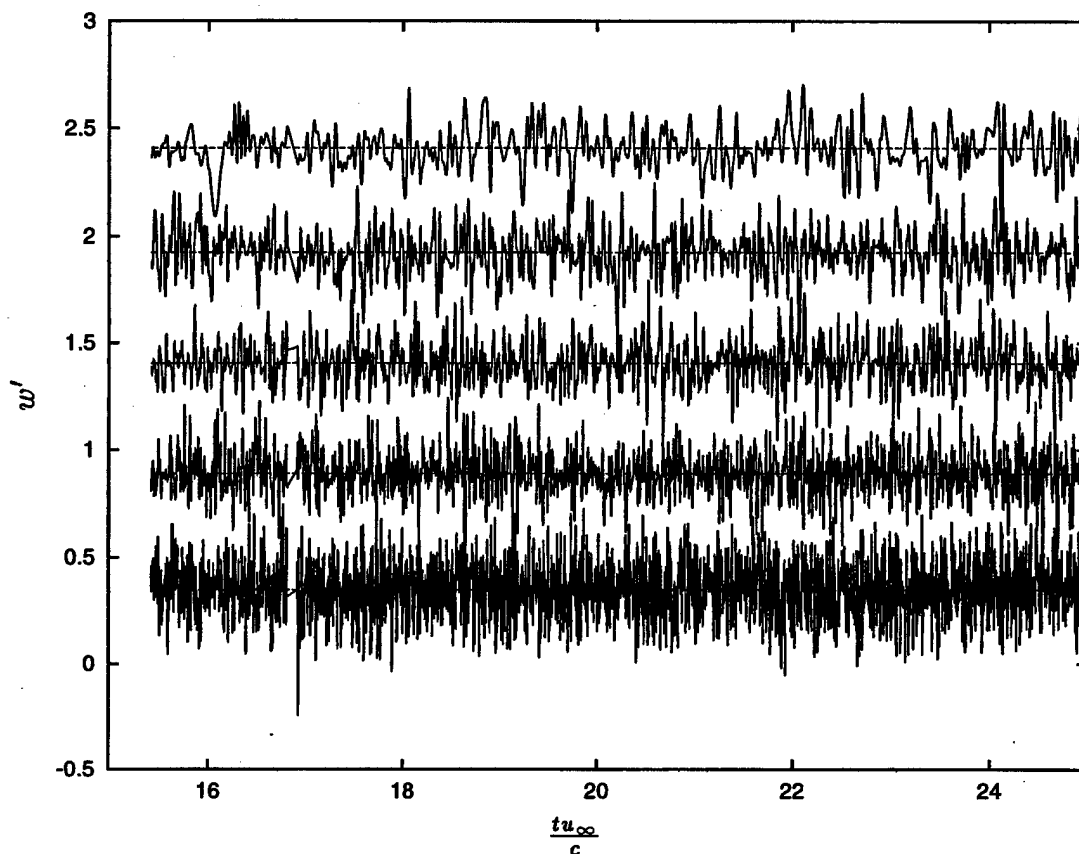


FIGURE 5. Time series of the spanwise velocity fluctuation as described in Fig. 4. Note that the top curve ($x/c = 0.95$) has a strong signal indicating a return of three-dimensionality in the separated region with the increased domain width.

3.2 Higher order methods

Given the number of points that are required to obtain a grid-independent solution, it seems clear that higher order methods should be explored. This is straightforward, but non-trivial, to do with the finite element method. There are two benefits to higher order methods besides the obvious one of higher accuracy. First, the higher order methods will have a more complete representation of the residual error of the discrete approximation and, therefore, the scheme will be less dissipative. Second, alternative filters, described in Jansen (1994), can be implemented and tested. It is difficult to predict at this time if the method will lose computational efficiency when extended to higher order.

3.3 Computational platform change

In the past year the code has been ported to the IBM SP2 (see Bastin 1996 for details). This port involved the use of MPI, a communication standard that is more widely used than that of the original code, which should make the port to other platforms reasonably simple. In the coming year more effort will be applied in this area to try to take advantage of the changing computational resources available for

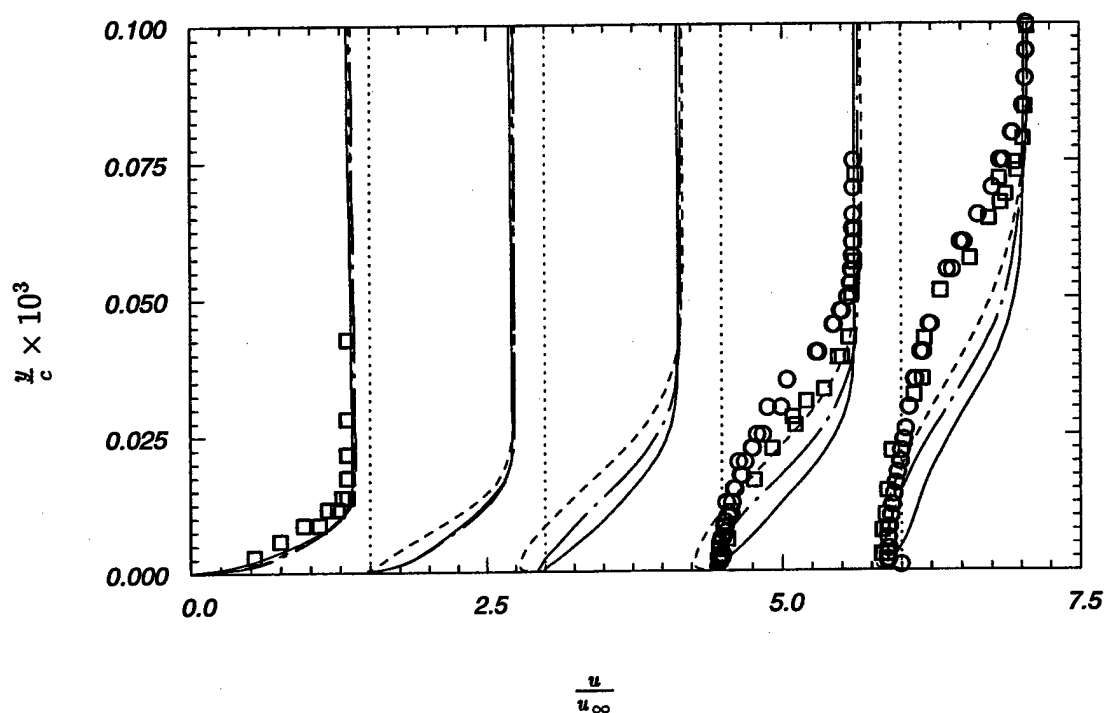


FIGURE 6. Profiles of tangential velocity component at various positions along the airfoil surface ($x/c = 0.59, 0.066, 0.78, 0.82, 0.95$). Solutions correspond to: without wind tunnel walls or transition strip —, with wind tunnel walls and transition strip ($W/c = 0.025$) ----, with wind tunnel walls and transition strip ($W/c = 0.05$) — · —, Wadcock \square , Hastings and Williams \circ .

this type of simulation, thereby expediting its progress.

REFERENCES

- BASTIN, F. 1996 Jet noise using large eddy simulation. *Annual Research Briefs 1996*. Center for Turbulence Research, NASA Ames/Stanford Univ.
- COLES, D., & WADCOCK, A. J. 1979 A flying-hot-wire study of two-dimensional mean flow past an NACA 4412 airfoil at maximum lift. *AIAA J.* **17**, 321.
- HASTINGS, R. C. & WILLIAMS, B. R. 1987 Studies of the flow field near a NACA 4412 aerofoil at nearly maximum lift. *Aero. J.* **91**, 29.
- JANSEN, K. 1994 Unstructured grid large eddy simulation of flow over an airfoil. *Annual Research Briefs 1994*. Center for Turbulence Research, NASA Ames/Stanford Univ., 161-174.
- JANSEN, K. 1995 Preliminary large-eddy simulations of flow around a NACA 4412 airfoil using unstructured grids. *Annual Research Briefs 1995*. Center for Turbulence Research, NASA Ames/Stanford Univ., 61-72.
- JANSEN, K., JOHAN, Z., & HUGHES, T. J. R. 1993 Implementation of a one-equation turbulence model within a stabilized finite element formulation of a

symmetric advective-diffusive system. *Comp. Meth. Appl. Mech. Eng.* **105**, 405.

JOHAN, Z., HUGHES, T. J. R., MATHUR, K. K., & JOHNSON, S. L. 1992 A data parallel finite element method for computational fluid dynamics on the Connection Machine system. *Comp. Meth. Appl. Mech. Eng.* **99**, 113.

WADCOCK, A. J. 1987 Investigation of low-speed turbulent separated flow around airfoils. *NACA CR 177450*.